Thermophoretic and Brownian diffusions in couple stress alumina–water nanofluid flow with Soret-Dufour and nonlinear radiation effects over a curved oscillatory stretching surface

[a]Muhammad Imran[*], [a]Muhammad Naveed, and [a]Waqas Ahmad

[a]Department of Mathematics, Division of Science and Technology,
University of Education Lahore 54770, Pakistan

Abstract: This study investigates the combined effects of Soret and Dufour phenomena on the hydrothermal transport of an alumina–water couple stress nanofluid, modeled using the Buongiorno nanofluid framework that incorporates Brownian motion and thermophoretic diffusion mechanisms. The fluid motion is considered over a curved oscillatory stretching surface, representing an important class of configurations in industrial and biomedical heat transport applications, including cooling technologies, thermal energy storage, and advanced process engineering systems. The governing model is established through a system of coupled nonlinear partial differential equations (PDEs) describing momentum, energy, and nanoparticle concentration fields. Nonlinear radiative heat transfer is incorporated via the Rosseland approximation to capture the influence of high-temperature thermal radiation. Suitable similarity transformations are used to transform the governing flow equations into a nonlinear dimensionless set of partial differential equations. The obtained equations are then solved analytically by incorporating the homotopy analysis method (HAM) to establish high accuracy and convergence control. Parametric examination reveals that the amplitude of velocity decreases with increasing the magnetic parameter, radius of curvature, nanoparticle volume fraction, and couple stress parameter. Furthermore, the temperature distribution increases with higher Dufour number and nanoparticle volume fraction. In general, the current study highlights the noteworthy interaction of coupled transport phenomena and alumina nanoparticles on flow, heat, and mass transfer characteristics. The novelty of this study lies in the simultaneous consideration of nonlinear radiation, Soret–Dufour effects, and curved oscillatory stretching surfaces in a couple-stress nanofluid, providing a new insight beyond existing literature for advanced thermal management system design.

Keywords: Curved oscillatory stretching surface, alumina-water nanofluid, couple stress fluid, nonlinear radiation, thermophoretic diffusion and Brownian motion, Soret-Dufour effect

1. Introduction

In past years, investigators and researchers have gradually focused on examining the nanofluids due to their notable characteristics to increase both flow phenomenon and rate of heat and mass transfer. This increasing interest rises from the higher thermophysical properties reported by nanoparticles, which considerably increase the efficiency of conventional fluids. Among many

[*] Corresponding Author. Tel.: +92 312 6490512

e-mail address: imran@ue.edu.pk (Muhammad Imran)

nanomaterials, alumina nanoparticles are mostly important due to their chemical stability, smooth dispersion, and high thermal conductivity which mutually boost the heat and mass transfer rate in base fluid. Nanomaterials have established wide ranging physical applications across various fields, including chemical processing, advanced thermal transport systems, nuclear technologies, device cooling and energy generation as well as in the fields of biomedical applications such as advanced diagnostic platforms, cancer hyperthermia treatment, targeted drug delivery and bio-imaging. The significant of nanofluids thus signifies a major advancement in thermal engineering and industrial applications. Choi [1] first introduced the term "nanofluids". These advanced heat transfer media (nanofluids) are engineered by dispersing nanoscale solid particles such as metals, metal oxides, or carbon-based nanomaterials into traditional base fluids like water, ethylene glycol, or oil. Nanofluids are employed in nuclear reactors, hybrid machines, solar water heating, transformer oil, and refrigeration, etc. Ragulkumar et al. [2] investigated nanofluid flow via a cone and determined the effects of radiation and chemical reaction. Imran et al. [3] attempted heat transport analysis in the oscillatory flow of hybrid nanofluid on a curvy sheet. Mohana and Kumar [4] studied hydromagnetic Cu-water nanofluid motion towards a stretched sheet with heat production. Bioconvective and chemically reactive flow of hybrid nano liquid via a curvy oscillating sheet was analyzed by Naveed et al. [5]. Syam et al. [6] analyzed the magnetized flow of nanofluid past a permeable sheet. To develop the flow model for microscale transport phenomena in nanofluids, the Buongiorno nanofluid model [7] is widely utilized. This model incorporates the influences of thermophoresis and Brownian diffusions which characterizes the random movement of nanoparticles. The random movement of nanoparticles results in enhancing energy exchange through particle diffusion, whereas thermophoresis pushes the nanoparticles from hotter to colder regions due to temperature gradients which significantly affecting both heat and mass transfer characteristics. So this nanofluid model provides a more comprehensive and realistic demonstration of nanofluid behavior as compared to conventional approaches. Ahmad et al. [8] studied the characteristics of Brownian motion and thermophoresis effects in the curvilinear flow of Williamson fluid. Imran and Naveed [9] attempted a numerical study to calculate the significance of activation energy along with thermophoresis and Brownian motion on Carreau fluid via a curved wall. The outcomes of thermophoretic and Brownian movement on the flow of Maxwell fluid utilizing an improved form of Fourier's and Fick's theory were accessed by Ali et al. [10]. Sankaralingam et al. [11] considered features of heat and mass transfer on magnetized flow of Powell-Eyring nanofluid with Brownian motion and thermophoresis effects. A wide range of studies investigating nanofluid flow over divergent stretching geometries can be found in the literature [12–18].

Numerous daily life fluids, such as blood, ketchup, yoghurt, mud, polymer melts, clay coatings, molten plastics, apple sauce, greases, and certain oils, are categorized as non-Newtonian liquids. Unlike Newtonian fluids, these liquids exhibit a complex relationship between shear stress and strain rate, meaning that Newton's law of viscosity does not adequately describe their behavior. The distinct characteristics of non-Newtonian fluids which has encouraged extensive research into the flow behavior cannot be examined by a single constitutive equation. These fluids have extensive practical applications across the fields in bioengineering, polymer manufacturing, chemical industries, plastic foam production, nuclear and petroleum

processing. Different mathematical models, depending on the specific physical properties of the fluid have been developed to deliberate their flow characteristics. Among the various classes of non-Newtonian models, couple stress fluid represents a notable class of non-Newtonian fluids which was first examined by Stokes [19]. The idea of couple stress fluid model extends the classical viscous model by incorporating body couples and micro rotational effects in an anti-symmetric stress tensor. This modification improves the order of the momentum equations from second to fourth by allowing the model to capture rotational interactions between fluid particles. Examples of couple stress fluids include lubricants, blood and colloidal suspensions which often exhibit synthetic and electro-rheological characteristics. Alabdan et al. [20] has examined the bioconvective flow of couple stress fluid to examine the impacts of time-dependent viscosity on an oscillatory surface. Mahesh et al. [21] studied the impacts of viscous dissipation in the thermally radiative couple stress flow of hybrid nano fluid on a permeable surface. The influence of various physical phenomena for couple stress fluids over different flow geometries has analyzed by various researchers see articles [22-25] and reference therein.

Boundary layer flows across a curved stretching surface have developed as an important research direction due to their extensive practical applications in engineering and industrial processes. Examples include glass molding, metallurgy, oil recovery, polymer extrusion, and paper manufacturing, where precise control of motion of the fluid and heat transfer near surface is important for ensuring the final quality of the product. Furthermore, the stretching motion of the surface consists of dynamics of complex fluid behavior, inducing shear stress, temperature and mass transport characteristics. Motivated by these physical applications, researchers have examined boundary layer flows across a stretching surface with different velocity profiles, such as exponential, linear, nonlinear and oscillatory stretching. From the aforesaid velocities, the oscillatory stretching holds particular importance because of the time dependent periodic motion introduces unsteady flow, shear layers and fluctuating thermal and solutal boundary layers. Such oscillations are particularly relevant in procedures where pulsatile forcing is employed to improve mixing, regulate heat transfer rates. Furthermore, the inclusion of additional physical effects such as effects of magnetic fields, linear and nonlinear thermal radiation and non-Newtonian rheology has made the study more realistic, thereby providing deeper insights into physical engineering applications. So, investigating these flows under different geometrical and physical conditions remains vital for optimizing industrial processes. A comprehensive study of the flow and transport phenomena across a curved stretching surface with oscillating, linear, nonlinear, and exponential stretching conditions has been reported in [26–35].

The transport mechanism consists of both heat and mass transfer play a important role in the boundary layer flows specially in systems consists of multicomponent fluids, thermal processing and chemical reactions. In addition to conventional energy and species transport, the Soret (thermal diffusion) and Dufour (diffusion-thermos) effects introduce important cross-diffusion mechanisms that significantly influence thermal and concentration boundary layers. The Soret effect produces a species flux due to temperature gradients, while the Dufour effect produces additional heat flux driven by concentration gradients. The study of these coupled

phenomena is extremely significant in physical applications such as food processing (e.g., freezing, baking and drying), packed sphere systems used in cooling towers and chemical reactors, fiber and polymer production, high-temperature geoscience systems and membrane separation processes. These effects are often neglected by various researchers due to their comparatively smaller magnitude as compared to Fourier and Fick's diffusion laws. Moreover, the Soret and Dufour effects become non-negligible in transport of nanofluids, porous media flows, hydrology and nuclear waste management. Their presence in the flow over a curved and stretchable surfaces provides more realistic insights into the interaction of momentum, thermal and solutal boundary layers. Shilpa et al. [36] examined the consequences of Dufour and Soret on mixed convection flow of couple stress fluid via a vertical channel. Islam et al. [37] studied the impacts of Dufour-Soret in the flow across a convective surface triple diffusion and magnetic field. Examination of bioconvective flow of micropolar nanofluid across a stretching surface with Dufour and Soret effects was carried out by Farooq et al. [38]. Nagari et al. [39] computed an analytical study to study the impacts of Soret-Dufour in the flow of Casson fluid on a stretching surface.

The study of impacts of nonlinear thermal radiation plays a significant role in high temperature heat transfer processes, where the classical linear approximation of radiative heat transfer becomes inadequate. In linear radiative heat transfer models, we assumed direct proportionality between temperature difference and radiative heat flux. However, in nonlinear thermal radiation depicts the temperature-dependent nature of thermal emission which often described through the Rosseland approximation. This consequences in a radiative heat flux proportional to the fourth power of temperature, which as a results introducing nonlinearity into the energy equation. The condition becomes even more important in electrically conducting fluids under the impact of applied magnetic fields. By incorporating nonlinear thermal radiation in such flows is vital for correctly predicting the thermal performance of engineering systems, such as plasma applications, thermal processing units, MHD power generators, aerospace vehicles exposed to re-entry heating, nuclear reactors and electronic cooling devices. In nanofluid flow, the combined impacts of nonlinear thermal radiation and magnetic fields considerably modify the thermal boundary layer and also enhance the heat transport mechanism to provide better control over high-temperature industrial processes. Reddy et al. [40] has examined the influence of nonlinear thermal radiation and magnetic field in the flow of Carreau and Casson fluids on a vertical porous sheet. Sulochana et al. [41] has carried out a study to examine the effects of activation energy and nonlinear thermal radiation in the bioconvective magnetized flow of non-Newtonian nanofluid on a surface. Anjum et al. [42] analyzed the features of nonlinear radiation and heat production in a hydromagnetic hybrid nanofluid past a stretchy sheet. Ganji et al. [43] detected the effects of nonlinear radiation and entropy production in the magnetized flow of nanofluid over a stretchable sheet.

The present work fills a critical research gap by investigating the hydrothermal transport of an alumina–water couple stress nanofluid over a curved oscillatory stretching surface while accounting for nonlinear radiation, magnetic field, Soret–Dufour cross-diffusion, Brownian motion, and thermophoretic diffusion within the Buongiorno framework. The literature survey reveals that most of the researchers have mainly focused on flat or simply stretching surfaces

with linear radiation approximations and a single transport mechanism. This led to a limited understanding of how these physical parameters simultaneously impact the boundary layer flows in oscillatory curved geometries. Furthermore, the inclusion of couple stress parameter, the current study focuses on the micro-rotational effects and higher-order stresses which often encountered in biofluids, suspensions, and lubricants, thus providing a more realistic description of non-Newtonian nanofluids. The existence of the nonlinear thermal radiation ensures an exact depiction of high temperature systems, while the inclusion of Soret and Dufour effects highlights important cross diffusion phenomena relevant to chemical and food systems. The formulated nonlinear PDEs are reduced to a dimensionless system. Then the obtained equations are solved analytically by using (HAM). This combined framework not only advances theoretical insights into coupled momentum–thermal–solutal interactions but also provides engineering guidelines for enhancing heat and mass transfer in advanced industrial and biomedical applications, thermal energy storage, including electronic cooling, and targeted therapeutic processes.

2. Problem explanation

A laminar, magnetized, time-dependent, and incompressible couple stress nano liquid flow past a stretchy curvy oscillatory wall that twisted in the shape of a semi-circle with radius $\bar{C}_\alpha$ is addressed. The physical model and coordinate system of the present problem are depicted in Figure 1. The to-and-fro motion of the sheet along the axial direction $\bar{x}_1$ due to the velocity $\bar{w}_1 = \bar{d}\,\bar{x}_1 \sin \bar{\varpi} \bar{t}$ is counted as the source of the flow scheme. Here $\bar{\varpi}$ and $\bar{d}$ are the oscillating frequency and stretched rate of the wall. The effects of the normally applied magnetic field of strength B_0 are ignored by supposing very low Reynolds numbers. Let $\bar{T}_w$ and $\bar{C}_w$ are the temperature and concentration of nanoparticles at the wall, while $\bar{T}_\infty$ is the ambient temperature and $\bar{C}_\infty$ signify the ambient nanoparticle concentration $\bar{T}_\infty < \bar{T}_w$ and $\bar{C}_\infty < \bar{C}_w$. The governing equations for the designated flow problem are labeled by

$$\nabla.\mathbf{W} = 0, \tag{1}$$

$$\left(\frac{\partial \mathbf{W}}{\partial \bar{t}} + (\mathbf{W}.\nabla)\mathbf{W}\right) = -\frac{1}{\bar{\rho}_{nf}}\nabla \bar{p} + \frac{\bar{\mu}_{nf}}{\bar{\rho}_{nf}}\nabla^2 \mathbf{W} - \frac{\bar{\eta}_0}{\bar{\rho}_{nf}}\nabla^4 \mathbf{W} + \frac{1}{\bar{\rho}_{nf}}(\mathbf{J}\times\mathbf{B}), \tag{2}$$

$$\left(\frac{\partial \bar{T}}{\partial \bar{t}} + (\mathbf{W}.\nabla)\bar{T}\right) = \frac{\bar{k}_{nf}}{(\bar{\rho}c_p)_{nf}}\nabla^2 \bar{T} + \frac{1}{(\bar{\rho}c_p)_{nf}}\nabla.\left(\left(\frac{16\bar{\sigma}_\alpha \bar{T}^3}{3\bar{\kappa}_\beta}\right)\nabla \bar{T}\right) + \frac{\bar{\rho}_f \bar{D}_T \bar{k}_T}{\bar{c}_{\bar{s}}(\bar{\rho}c_p)_{nf}}\nabla^2 \bar{C}$$
$$+ \frac{(\bar{\rho}c_p)_s}{(\bar{\rho}c_p)_{nf}}\left(\bar{D}_\alpha(\nabla \bar{T}.\nabla \bar{C}) + \left(\frac{\bar{D}_T}{\bar{T}_\infty}\right)(\nabla \bar{T}.\nabla \bar{T})\right), \tag{3}$$

$$\left(\frac{\partial \bar{C}}{\partial \bar{t}}+\left(\mathbf{W}.\nabla\right)\bar{C}\right)=\bar{D}_{\alpha}\nabla^{2}\bar{C}+\frac{\bar{D}_{T}\bar{k}_{T}}{\bar{T}_{m}}\nabla^{2}\bar{T}+\frac{\bar{D}_{T}}{\bar{T}_{\infty}}\nabla^{2}\bar{T}, \tag{4}$$

here $\mathbf{W}$ signify the velocity vector, $\bar{k}_{nf}$ is the thermal conductivity of the nanofluid, ∇^2 the Laplacian operator, $\bar{D}_{\alpha}$ signify the Brownian diffusion coefficient, $\mathbf{B}$ depicts the magnetic flux vector, $\bar{p}$ is the pressure, $\bar{T}$ is the temperature, $\bar{\eta}_0$ is the couple stress fluid constant, $\bar{\sigma}_{\alpha}$ signify the Stefan-Boltzmann coefficient, $\bar{\mu}_{nf}$ is the nanofluid dynamic viscosity, $\bar{T}_m$ represents the mean liquid temperature, $\bar{c}_{\bar{s}}$ is the concentration susceptibility, $\bar{k}_T$ is the relation of thermal diffusion, $\left(\bar{\rho}c_p\right)_{nf}$ is the heat capacitance of the nanofluid, $\bar{\rho}_{nf}$ is the nanofluid density, $\bar{D}_T$ is the thermophoretic diffusion, $\bar{\kappa}_{\beta}$ denotes the mean absorption coefficient, $\bar{\rho}_f$ is the base fluid density, $\bar{C}$ signify the concentration, and $\mathbf{J}$ is the current density, which is designated as

$$\mathbf{J}=\bar{\sigma}_{nf}\left(\mathbf{W}\times\mathbf{B}\right), \tag{5}$$

For the current flow problem, we consider a velocity field of the form

$$\mathbf{W}=\left(\bar{w}_2\left(\bar{x}_1,\bar{t},\bar{x}_2\right),\bar{w}_1\left(\bar{x}_1,\bar{t},\bar{x}_2\right),0\right),\ \bar{T}=\bar{T}\left(\bar{x}_1,\bar{t},\bar{x}_2\right),\ \bar{C}=\bar{C}\left(\bar{x}_1,\bar{t},\bar{x}_2\right), \tag{6}$$

where $\bar{\sigma}_{nf}$ is the electrical conductivity of the nanofluid and $\left(\bar{w}_1,\bar{w}_2\right)$ are the liquid velocity parts along $\left(\bar{x}_1,\bar{x}_2\right)$ directions. By incorporating Eqs. (5)-(6) along with boundary layer approximations, the governing Eqs. (1)-(4) can be expressed in a curvilinear coordinate system as [21, 23]

$$\frac{\partial \bar{w}_2}{\partial \bar{x}_2}+\frac{\bar{w}_2}{\left(\bar{C}_{\alpha}+\bar{x}_2\right)}+\frac{\partial \bar{w}_1}{\partial \bar{x}_1}\frac{\bar{C}_{\alpha}}{\left(\bar{C}_{\alpha}+\bar{x}_2\right)}=0, \tag{7}$$

$$\frac{\partial \bar{p}}{\partial \bar{x}_2}=\frac{\bar{\rho}_{nf}\bar{w}_1^{\,2}}{\left(\bar{C}_{\alpha}+\bar{x}_2\right)}, \tag{8}$$

$$\frac{\partial \bar{w}_1}{\partial \bar{t}}+\frac{\bar{w}_2\,\bar{w}_1}{\bar{x}_2+\bar{C}_\alpha}+\frac{\partial \bar{w}_1}{\partial \bar{x}_2}\bar{w}_2+\frac{\partial \bar{w}_1}{\partial \bar{x}_1}\frac{\bar{C}_\alpha \bar{w}_1}{\left(\bar{x}_2+\bar{C}_\alpha\right)}=-\frac{1}{\bar{\rho}_{nf}}\frac{\bar{C}_\alpha}{\left(\bar{x}_2+\bar{C}_\alpha\right)}\frac{\partial \bar{p}}{\partial \bar{x}_1}-\frac{\bar{\sigma}_{nf}}{\bar{\rho}_{nf}}B_0^2\bar{w}_1$$
$$-\frac{\bar{\eta}_0}{\bar{\rho}_{nf}}\left(\frac{\partial^4 \bar{w}_1}{\partial \bar{x}_2{}^4}+\frac{3\partial \bar{w}_1}{\left(\bar{x}_2+\bar{C}_\alpha\right)^3\partial \bar{x}_2}-\frac{3}{\left(\bar{x}_2+\bar{C}_\alpha\right)^2}\frac{\partial^2 \bar{w}_1}{\partial \bar{x}_2{}^2}+\frac{2}{\bar{x}_2+\bar{C}_\alpha}\frac{\partial^3 \bar{w}_1}{\partial \bar{x}_2{}^3}-\frac{3\bar{w}_1}{\left(\bar{x}_2+\bar{C}_\alpha\right)^4}\right) \tag{9}$$
$$+\frac{\bar{\mu}_{nf}}{\bar{\rho}_{nf}}\left(\frac{\partial^2 \bar{w}_1}{\partial \bar{x}_2{}^2}+\frac{\partial}{\partial \bar{x}_2}\left(\frac{\bar{w}_1}{\left(\bar{x}_2+\bar{C}_\alpha\right)}\right)\right),$$

$$\frac{\partial \bar{T}}{\partial \bar{t}}+\frac{\bar{w}_1\bar{C}_\alpha\partial \bar{T}}{\left(\bar{x}_2+\bar{C}_\alpha\right)\partial \bar{x}_1}+\bar{w}_2\frac{\partial \bar{T}}{\partial \bar{x}_2}=\frac{\bar{k}_{nf}}{\left(\bar{\rho}c_p\right)_{nf}}\left(\frac{\partial^2 \bar{T}}{\partial \bar{x}_2^2}+\frac{\partial \bar{T}}{\left(\bar{x}_2+\bar{C}_\alpha\right)\partial \bar{x}_2}\right)$$
$$+\frac{1}{\left(\bar{\rho}c_p\right)_{nf}\left(\bar{x}_2+\bar{C}_\alpha\right)}\frac{\partial}{\partial \bar{x}_2}\left(\left(\bar{x}_2+\bar{C}_\alpha\right)\left(\frac{16\bar{\sigma}_\alpha}{3\bar{\kappa}_\beta}\right)\frac{\partial \bar{T}}{\partial \bar{x}_2}\right)+\frac{\bar{\rho}_f\bar{D}_T\bar{k}_T}{\bar{c}_{\bar{s}}\left(\bar{\rho}c_p\right)_{nf}}\left(\frac{\partial^2 \bar{C}}{\partial \bar{x}_2^2}+\left(\frac{1}{\left(\bar{x}_2+\bar{C}_\alpha\right)}\right)\frac{\partial \bar{C}}{\partial \bar{x}_2}\right) \tag{10}$$
$$+\frac{\left(\bar{\rho}c_p\right)_s}{\left(\bar{\rho}c_p\right)_{nf}}\left(\bar{D}_\alpha\left(\frac{\partial \bar{T}}{\partial \bar{x}_2}\frac{\partial \bar{C}}{\partial \bar{x}_2}\right)+\left(\frac{\bar{D}_T}{\bar{T}_\infty}\right)\left(\frac{\partial \bar{T}}{\partial \bar{x}_2}\right)^2\right),$$

$$\frac{\partial \bar{C}}{\partial \bar{t}}+\left(\frac{\bar{C}_\alpha\bar{w}_1}{\bar{C}_\alpha+\bar{x}_2}\right)\frac{\partial \bar{C}}{\partial \bar{x}_1}+\bar{w}_2\frac{\partial \bar{C}}{\partial \bar{x}_2}=\bar{D}_\alpha\left(\frac{\partial^2 \bar{C}}{\partial \bar{x}_2^2}+\left(\frac{1}{\bar{C}_\alpha+\bar{x}_2}\right)\frac{\partial \bar{C}}{\partial \bar{x}_2}\right)+\frac{\bar{D}_T\,\bar{k}_T}{\bar{T}_m}\left(\frac{\partial^2 \bar{T}}{\partial \bar{x}_2^2}+\frac{1}{\left(\bar{C}_\alpha+\bar{x}_2\right)}\frac{\partial \bar{T}}{\partial \bar{x}_2}\right) \tag{11}$$
$$+\frac{\bar{D}_T}{\bar{T}_\infty}\left(\frac{\partial^2 \bar{T}}{\partial \bar{x}_2^2}+\frac{1}{\left(\bar{C}_\alpha+\bar{x}_2\right)}\frac{\partial \bar{T}}{\partial \bar{x}_2}\right),$$

With boundary conditions [23]

$$\left.\begin{aligned}&\bar{w}_2=0,\quad \bar{w}_1=\bar{d}\,\bar{x}_1\sin\bar{\omega}\bar{t},\ \frac{\partial^2 \bar{w}_1}{\partial \bar{x}_2^2}\to 0,\ \frac{\partial^3 \bar{w}_1}{\partial \bar{x}_2^3}\to 0,\ \bar{C}=\bar{C}_w,\ \bar{T}=\bar{T}_w\ \text{ at }\bar{x}_2=0,\\&\bar{T}\to\bar{T}_\infty,\ \frac{\partial \bar{w}_1}{\partial \bar{r}}\to 0,\ \bar{C}\to\bar{C}_\infty,\quad \bar{w}_1\to 0,\quad \text{as }\bar{x}_2\to\infty.\end{aligned}\right\} \tag{12}$$

The thermophysical features, including density, dynamic viscosity, electrical and thermal conductivity, and specific heat capacitance for nanofluid, are specified in Eq. (13), respectively, as presented in [3]. Additionally, the thermophysical values of the base liquid and nanoparticles are listed in Table 1.

$$\left.\begin{aligned}&\bar{\rho}_{nf}=\varphi\bar{\rho}_s+(1-\varphi)\bar{\rho}_f,\ \bar{\mu}_{nf}=\frac{\bar{\mu}_f}{(1-\varphi)^{2.5}},\ \bar{\sigma}_{nf}=\frac{\bar{\sigma}_s+2\bar{\sigma}_f-2\varphi\left(\bar{\sigma}_f-\bar{\sigma}_s\right)}{\bar{\sigma}_s+2\bar{\sigma}_f+\varphi\left(\bar{\sigma}_f-\bar{\sigma}_s\right)}\times\bar{\sigma}_f,\\&\left(\bar{\rho}c_p\right)_{nf}=\varphi\left(\bar{\rho}c_p\right)_s+(1-\varphi)\left(\bar{\rho}c_p\right)_f,\ \bar{k}_{nf}=\frac{\bar{k}_s+2\bar{k}_f-2\varphi\left(\bar{k}_f-\bar{k}_s\right)}{\bar{k}_s+2\bar{k}_f+\varphi\left(\bar{k}_f-\bar{k}_s\right)}\times\bar{k}_f\end{aligned}\right\} \tag{13}$$

Now commencing the subsequent dimensionless variables as

$$\sqrt{\frac{\bar{d}}{\bar{\nu}_f}}\bar{x}_2=\bar{\chi},\ \bar{d}\,\bar{x}_1\bar{F}_{\bar{\chi}}\left(\bar{\chi},\bar{\tau}\right)=\bar{w}_1,\ \frac{-\bar{C}_\alpha}{\bar{C}_\alpha+\bar{x}_2}\sqrt{\bar{d}\,\bar{\nu}_f}\,\bar{F}\left(\bar{\chi},\bar{\tau}\right)=\bar{w}_2,$$
$$\bar{t}\,\varpi=\bar{\tau},\ \bar{\rho}_f\bar{d}^2\,\bar{x}_1^{\,2}\bar{P}\left(\bar{\chi},\bar{\tau}\right)=\bar{p},\ \bar{\Phi}\left(\bar{\chi},\bar{\tau}\right)=\left(\bar{C}-\bar{C}_\infty\right)/\left(\bar{C}_w-\bar{C}_\infty\right), \tag{14}$$
$$\bar{\Theta}\left(\bar{\chi},\bar{\tau}\right)=\left(\bar{T}-\bar{T}_\infty\right)/\left(\bar{T}_w-\bar{T}_\infty\right),\ \bar{T}=\bar{T}_\infty\left(1+\left(\gamma-1\right)\bar{\Theta}\left(\bar{\chi},\bar{\tau}\right)\right),\ \gamma=\left(\bar{T}_w/\bar{T}_\infty\right)>1.$$

In the above Eq. (14) $\bar{F}_{\bar{\chi}}$, $\bar{F}$, $\bar{\Theta}$ and $\bar{\Phi}$ are the dimensionless horizontal and vertical velocity parts, temperature, and concentration of the fluid, $\bar{\nu}_f$ is the kinematic viscosity of the base fluid, γ is the temperature ratio variable, $\bar{C}_\alpha$ and $\bar{t}$ are the radius of curvature and time, $\bar{\chi}$ and $\bar{\tau}$ are the dimensionless similarity variables, and $\bar{P}$ is the dimensionless pressure. In view of Eq. (14), Eq. (7) is verified identically, and the rest of the Eqs. (8)-(11) become

$$\frac{E_{11}\bar{F}_{\bar{\chi}}^{\,2}}{C_1+\bar{\chi}}=\bar{P}_{\bar{\chi}}, \tag{15}$$

$$\bar{P}\left(\bar{\chi},\bar{\tau}\right)=\frac{E_{11}}{E_{12}}\left(\frac{\left(C_1+\bar{\chi}\right)\bar{F}_{\bar{\chi}\bar{\chi}\bar{\chi}}}{2C_1}-\frac{\bar{F}_{\bar{\chi}}}{2C_1\left(C_1+\bar{\chi}\right)}+\frac{\bar{F}_{\bar{\chi}\bar{\chi}}}{2C_1}\right)-\frac{\left(C_1+\bar{\chi}\right)E_{11}S\bar{F}_{\bar{\chi}\bar{\tau}}}{2C_1}$$
$$-\lambda\left(\frac{\bar{F}_{\bar{\chi}\bar{\chi}\bar{\chi}\bar{\chi}\bar{\chi}}\left(C_1+\bar{\chi}\right)}{2C_1}-\frac{3}{2C_1}\frac{\bar{F}_{\bar{\chi}\bar{\chi}\bar{\chi}}}{\left(C_1+\bar{\chi}\right)}+\frac{\bar{F}_{\bar{\chi}\bar{\chi}\bar{\chi}\bar{\chi}}}{C_1}+\frac{3}{2C_1}\frac{\bar{F}_{\bar{\chi}\bar{\chi}}}{\left(C_1+\bar{\chi}\right)^2}+\frac{3}{2C_1}\frac{\bar{F}_{\bar{\chi}}}{\left(C_1+\bar{\chi}\right)^3}\right) \tag{16}$$
$$+\frac{\bar{F}\,E_{11}\bar{F}_{\bar{\chi}}}{2\left(C_1+\bar{\chi}\right)}-\frac{\left(C_1+\bar{\chi}\right)\bar{F}_{\bar{\chi}}\bar{\sigma}_{nf}M^2}{2C_1\bar{\sigma}_f}+\frac{E_{11}}{2}\left(\bar{F}_{\bar{\chi}\bar{\chi}}-\bar{F}\,\bar{F}_{\bar{\chi}}^2\right),$$

$$\frac{\bar{k}_{nf}}{\bar{k}_f P_r E_{13}}\frac{1}{\left(C_1+\bar{\chi}\right)}\frac{\partial}{\partial\bar{\chi}}\left(\left(1+\frac{\bar{k}_f R_d}{\bar{k}_{nf}}\left(1+\left(\gamma-1\right)\bar{\Theta}\right)^3\right)\left(C_1+\bar{\chi}\right)\bar{\Theta}_{\bar{\chi}}\right)+\frac{D_u}{E_{13}}\left(\bar{\Phi}_{\bar{\chi}\bar{\chi}}+\frac{\bar{\Phi}_{\bar{\chi}}}{\left(C_1+\bar{\chi}\right)}\right)$$
$$+\frac{N_b\bar{\Phi}_{\bar{\chi}}\bar{\Theta}_{\bar{\chi}}}{E_{13}}+\frac{N_t\left(\bar{\Theta}_{\bar{\chi}}\right)^2}{E_{13}}+\frac{C_1\bar{\Theta}_{\bar{\chi}}\bar{F}}{\left(C_1+\bar{\chi}\right)}-S\bar{\Theta}_{\bar{\tau}}=0, \tag{17}$$

$$\frac{1}{L_e}\left(\bar{\Phi}_{\bar{\chi}\bar{\chi}}+\frac{\bar{\Phi}_{\bar{\chi}}}{\left(\bar{\chi}+C_1\right)}\right)+S_r\left(\bar{\Theta}_{\bar{\chi}\bar{\chi}}+\frac{\bar{\Theta}_{\bar{\chi}}}{\left(\bar{\chi}+C_1\right)}\right)+\frac{N_t}{N_b L_e}\left(\bar{\Theta}_{\bar{\chi}\bar{\chi}}+\frac{\bar{\Theta}_{\bar{\chi}}}{\left(\bar{\chi}+C_1\right)}\right)$$
$$+\left(\frac{C_1}{\left(C_1+\bar{\chi}\right)}\bar{F}\bar{\Phi}_{\bar{\chi}}-S\bar{\Phi}_{\bar{\tau}}\right)=0, \tag{18}$$

where, $\lambda\left(=\bar{\eta}_0\,\bar{d}/\bar{\rho}_f\bar{\nu}_f^2\right)$ the nondimensional couple stress parameter, $C_1\left(=\bar{C}_\alpha\sqrt{\bar{d}/\bar{\nu}_f}\right)$ radius of curvature variable, $N_t\left(=\left(\bar{\rho}c_p\right)_s\bar{D}_T\left(\bar{T}_w-\bar{T}_\infty\right)/\bar{\nu}_f\left(\bar{\rho}c_p\right)_f\bar{T}_\infty\right)$ the thermophoretic variable, $S\left(=\varpi/\bar{d}\right)$ the unsteady variable, constant, $P_r\left(=\left(\bar{\mu}c_p\right)_f/\bar{k}_f\right)$ the Prandtl number,

$M^2\left(=\bar{\sigma}_f B_0^2/\bar{\rho}_f \bar{d}\right)$ the magnetic parameter, $L_e\left(=\bar{\nu}_f/\bar{D}_\alpha\right)$ the Lewis number, $D_u\left(=\bar{D}_T\bar{k}_T\left(\bar{C}_w-\bar{C}_\infty\right)/\left(\bar{T}_w-\bar{T}_\infty\right)\bar{\nu}_f\bar{c}_{\bar{s}}\left(c_p\right)_{\bar{f}}\right)$ the Dufour number, $R_d\left(=16\bar{\sigma}_\alpha\bar{T}_\infty^3/3\bar{\kappa}_\beta\bar{k}_f\right)$ the radiation parameter, $N_b\left(=\left(\bar{\rho}c_p\right)_s\bar{D}_\alpha\left(\bar{C}_w-\bar{C}_\infty\right)/\bar{\nu}_f\left(\bar{\rho}c_p\right)_f\right)$ the Brownian variable, and $S_r\left(=\bar{D}_T\bar{k}_T\left(\bar{T}_w-\bar{T}_\infty\right)/\left(\bar{C}_w-\bar{C}_\infty\right)\bar{\nu}_f\bar{T}_m\right)$ the Soret parameter, respectively.

After the eradication of the pressure expression existing in Eqs. (15)-(16), the velocity equation is attained as

$$\frac{E_{11}}{E_{12}}\bar{F}_{\bar{\chi}\bar{\chi}\bar{\chi}\bar{\chi}\bar{\chi}}+\frac{2E_{11}}{E_{12}}\left(\frac{\bar{F}_{\bar{\chi}\bar{\chi}\bar{\chi}}}{C_1+\bar{\chi}}\right)-SE_{11}\left(\bar{F}_{\bar{\chi}\bar{\chi}\bar{\tau}}+\frac{\bar{F}_{\bar{\chi}\bar{\tau}}}{\left(C_1+\bar{\chi}\right)}\right)-\frac{E_{11}}{E_{12}}\frac{\bar{F}_{\bar{\chi}\bar{\chi}}}{\left(C_1+\bar{\chi}\right)^2}+\frac{E_{11}}{E_{12}}\frac{\bar{F}_{\bar{\chi}}}{\left(C_1+\bar{\chi}\right)^3}$$
$$+\frac{\bar{F}E_{11}\bar{F}_{\bar{\chi}\bar{\chi}\bar{\chi}}C_1}{\left(C_1+\bar{\chi}\right)}-\frac{E_{11}C_1}{\left(C_1+\bar{\chi}\right)^2}\bar{F}_{\bar{\chi}}\bar{F}_{\bar{\chi}\bar{\chi}}-\frac{C_1E_{11}}{\left(C_1+\bar{\chi}\right)^2}\left(\bar{F}_{\bar{\chi}}^2-\bar{F}_{\bar{\chi}\bar{\chi}}\bar{F}\right)-\left(\bar{F}_{\bar{\chi}\bar{\chi}}+\frac{\bar{F}_{\bar{\chi}}}{\left(C_1+\bar{\chi}\right)}\right)\frac{\bar{\sigma}_{nf}M^2}{\bar{\sigma}_f} \tag{19}$$
$$-\frac{C_1E_{11}\bar{F}_{\bar{\chi}}\bar{F}}{\left(C_1+\bar{\chi}\right)^3}-\lambda\left(\bar{F}_{\bar{\chi}\bar{\chi}\bar{\chi}\bar{\chi}\bar{\chi}\bar{\chi}}+3\left(\frac{3\bar{F}_{\bar{\chi}}}{\left(C_1+\bar{\chi}\right)^5}-\frac{3\bar{F}_{\bar{\chi}\bar{\chi}}}{\left(C_1+\bar{\chi}\right)^4}+\frac{2\bar{F}_{\bar{\chi}\bar{\chi}\bar{\chi}}}{\left(C_1+\bar{\chi}\right)^3}-\frac{\bar{F}_{\bar{\chi}\bar{\chi}\bar{\chi}\bar{\chi}}}{\left(C_1+\bar{\chi}\right)^2}+\frac{\bar{F}_{\bar{\chi}\bar{\chi}\bar{\chi}\bar{\chi}\bar{\chi}}}{\left(C_1+\bar{\chi}\right)}\right)\right)=0.$$

here E_{11}, E_{12}, and E_{13} are defined as

$$\left.\begin{aligned}E_{11}&=\left(1-\varphi\right)+\varphi\,\bar{\rho}_s/\bar{\rho}_f,\\E_{12}&=\left(1-\varphi\right)^{2.5}\left(\left(1-\varphi\right)+\varphi\,\bar{\rho}_s/\bar{\rho}_f\right),\\E_{13}&=\left(1-\varphi\right)+\varphi\left(\bar{\rho}c_p\right)_s/\left(\bar{\rho}c_p\right)_f,\end{aligned}\right\} \tag{20}$$

The relevant Bcs are

$$\left.\begin{aligned}&\bar{F}_{\bar{\chi}\bar{\chi}\bar{\chi}}\left(0,\bar{\tau}\right)=0,\ \bar{\Phi}\left(0,\bar{\tau}\right)=1,\bar{F}\left(0,\bar{\tau}\right)=0,\ \bar{\Theta}\left(0,\bar{\tau}\right)=1,\ \bar{F}_{\bar{\chi}\bar{\chi}\bar{\chi}\bar{\chi}}\left(0,\bar{\tau}\right)=0,\ \bar{F}_{\bar{\chi}}\left(0,\bar{\tau}\right)=sin\bar{\tau},\\&\bar{\Phi}\left(\infty,\bar{\tau}\right)=0,\ \bar{F}_{\bar{\chi}}\left(\infty,\bar{\tau}\right)=0,\quad\bar{F}_{\bar{\chi}\bar{\chi}}\left(\infty,\bar{\tau}\right)=0,\quad\bar{\Theta}\left(\infty,\bar{\tau}\right)=0.\end{aligned}\right\} \tag{21}$$

The relevant engineering quantities along the curvy wall are symbolized as

$$Nu_s=\frac{\bar{x}_2\,q_w}{\left(\bar{T}_w-\bar{T}_\infty\right)\bar{\kappa}_\beta},\quad\bar{C}_{\bar{F}}=\frac{\tau_{\bar{x}_1\bar{x}_2}}{\bar{\rho}_f\bar{u}_w^2},\quad Sh_s=\frac{\bar{x}_2\,j_w}{\left(\bar{C}_w-\bar{C}_\infty\right)\bar{D}_\alpha}, \tag{22}$$

here, q_w, j_w, and $\tau_{\bar{x}_1\bar{x}_2}$ are depicted by

$$q_w = -\bar{k}_{nf}\left(1+\frac{16\bar{\sigma}_\alpha T_\infty^3\left(1+(\gamma-1)\bar{\Theta}\right)^3}{3\bar{\kappa}_\beta \bar{k}_f}\frac{\bar{k}_f}{\bar{k}_{nf}}\right)\left.\frac{\partial \bar{T}}{\partial \bar{x}_2}\right|_{\bar{x}_2=0}, \quad j_w = -\left.\left(\bar{D}_\alpha \frac{\partial \bar{C}}{\partial \bar{x}_2}\right)\right|_{\bar{x}_2=0},$$

$$\tau_{\bar{x}_1\bar{x}_2} = \left.\left(\bar{\mu}_{nf}\left(\frac{\partial \bar{w}_1}{\partial \bar{x}_2}-\frac{\bar{w}_1}{\bar{C}_\alpha+\bar{x}_2}\right)-\bar{\eta}_0\left(\frac{\partial^3 \bar{w}_1}{\partial \bar{r}^3}-\frac{1}{\left(\bar{C}_\alpha+\bar{x}_2\right)^2}\frac{\partial \bar{w}_1}{\partial \bar{x}_2}+\frac{\bar{w}_1}{\left(\bar{C}_\alpha+\bar{x}_2\right)^3}\right)\right)\right|_{\bar{x}_2=0}, \tag{23}$$

In the above Eqs. (22)-(23) $\bar{C}_{\bar{F}}$, Nu_s, $\tau_{\bar{x}_1\bar{x}_2}$, q_w, j_w, Sh_s and $\bar{k}_f$ are the dimensionless skin friction coefficient, dimensionless local Nusselt number, shear stress, heat flux, mass flux, local Sherwood number, and thermal conductivity of the base fluid, respectively.

Making use of Eqs. (14)-(23), Eq. (22) reduces to

$$\bar{C}_{\bar{F}}\left(\sqrt{Re_s}\right) = \frac{1}{(1-\varphi)^{2.5}}\left(\bar{F}_{\bar{\chi}\bar{\chi}}(0,\bar{\tau})-\frac{\bar{F}_{\bar{\chi}}(0,\bar{\tau})}{C_1}\right)-\lambda\left(\bar{F}_{\bar{\chi}\bar{\chi}\bar{\chi}\bar{\chi}}(0,\bar{\tau})-\frac{\bar{F}_{\bar{\chi}\bar{\chi}}(0,\bar{\tau})}{C_1^2}+\frac{\bar{F}_{\bar{\chi}}(0,\bar{\tau})}{C_1^3}\right), \tag{24}$$

$$Nu_s/\sqrt{Re_s} = -\frac{\bar{k}_{nf}}{\bar{k}_f}\left(1+\frac{\bar{k}_f}{\bar{k}_{nf}}R_d\left(1+(\gamma-1)\bar{\Theta}\right)^3\right)\bar{\Theta}_{\bar{\chi}}(0,\bar{\tau}), \tag{25}$$

$$Sh_s/\sqrt{Re_s} = -\bar{\Phi}_{\bar{\chi}}(0,\bar{\tau}). \tag{26}$$

3. Explanation of Solution Method

This section focuses on the HAM solution technique, which is used to obtain the series solution of the established Eqs. (17)-(20). Owing to its strong capability in handling highly nonlinear and coupled differential equations, HAM has been widely used in fluid flow and heat and mass transfer analyses. Unlike traditional perturbation techniques and many numerical methods, this approach (HAM) does not depend on the existence of small or large physical parameters, which enhances its applicability to a wide range of practical problems. A distinctive feature of HAM is the inclusion of auxiliary convergence-control parameters, which allow explicit regulation of the convergence region and ensure the reliability and accuracy of the obtained series solutions. Furthermore, HAM yields a continuous analytical expression for the velocity, temperature and concentration distributions, helping in a clear assessment of the impacts of various pertinent physical parameters. These main features make HAM mainly suitable for examining complex transport phenomena in flow of non-Newtonian nanofluid on a curved oscillatory surface. The comprehensive procedural steps of the HAM method are illustrated in Figure 2 through a flow chart [5, 9].

The initial supposition and auxiliary linear operators are initiated as:

$$\bar{\Phi}_0(\bar{\chi},\bar{\tau})=\exp(-\bar{\chi}),\quad \bar{\Theta}_0(\bar{\chi},\bar{\tau})=\exp(-\bar{\chi}),$$
$$\bar{F}_0(\bar{\chi},\bar{\tau})=\frac{sin\bar{\tau}\left(12-12\exp(-\bar{\chi})+6\bar{\chi}\exp(-\bar{\chi})-\bar{\chi}^2\exp(-\bar{\chi})\right)}{6}, \tag{27}$$

$$\bar{L}_{\bar{\Phi}}(\bar{\Phi})=\frac{\partial^2\bar{\Phi}}{\partial\bar{\chi}^2}-\bar{\Phi},\qquad \bar{L}_{\bar{\Theta}}(\bar{\Theta})=\frac{\partial^2\bar{\Theta}}{\partial\bar{\chi}^2}-\bar{\Theta},$$
$$\bar{L}_{\bar{F}}(\bar{F})=\frac{\partial^6\bar{F}}{\partial\bar{\chi}^6}+\frac{\partial^5\bar{F}}{\partial\bar{\chi}^5}-2\frac{\partial^4\bar{F}}{\partial\bar{\chi}^4}-2\frac{\partial^3\bar{F}}{\partial\bar{\chi}^3}+\frac{\partial^2\bar{F}}{\partial\bar{\chi}^2}+\frac{\partial\bar{F}}{\partial\bar{\chi}}, \tag{28}$$

which hold the following outcomes

$$\bar{L}_{\bar{F}}\left[\bar{g}_2\exp(\bar{\chi})+\bar{g}_3\bar{\xi}\exp(\bar{\chi})+\left(\bar{g}_4+\bar{g}_5\bar{\chi}+\bar{g}_6\bar{\chi}^2\right)\exp(-\bar{\chi})+\bar{g}_1\right]=0,$$
$$\bar{L}_{\bar{\Theta}}\left[\bar{g}_7\exp(\bar{\chi})+\bar{g}_8\exp(-\bar{\chi})\right]=0, \tag{29}$$
$$\bar{L}_{\bar{\Phi}}\left[\bar{g}_9\exp(\bar{\chi})+\bar{g}_{10}\exp(-\bar{\chi})\right]=0,$$

here $\bar{g}_i\ (i=1\text{-}10)$ signify arbitrary constants.

4. Results and Discussions

The purpose of this section is to illustrate and interpret the graphical and tabular results corresponding to the influence of dissimilar governing flow parameters. In particular, the impacts of the couple stress parameter (λ), thermophoretic constant (N_t), the unsteady variable (S), radiation parameter (R_d), the Soret parameter (S_r), magnetic constant (M), Dufour number (D_u), solid volume fraction constant (φ), Prandtl number (P_r), dimensionless radius of curvature (C_1), Brownian movement variable (N_b), nondimensional temperature ratio constant (γ), and Lewis number (L_e) are investigated. Their respective effects on the temperature distribution, velocity field, concentration profile, pressure distribution, skin friction coefficient, and the local Sherwood and Nusselt numbers are thoroughly analyzed and discussed.

Figure 3(a-d) is made to interpret the consequences of diverse variables likely (C_1), (φ), (λ), and (M) on the profile of velocity $\bar{F}'(\bar{\chi},\bar{\tau})$ for $\bar{\tau}\in(0,10\pi)$. The results reveal that as the magnitude of these parameters increases, the amplitude of the velocity profile $\bar{F}'(\bar{\chi},\bar{\tau})$ diminishes gradually. Physically, the reduction in the velocity amplitude due to the magnetic parameter and couple stress variable reflects the enhanced resistive forces within the fluid, such as magnetic damping and couple stress resistance, which oppose the fluid motion. Such behavior is significant in engineering applications where flow resistance needs to be controlled, such as in lubrication technologies, magnetohydrodynamic pumps, and drag reduction systems.

Figures 4(a-b), 5(a-b), 6(a-b), and 7(a-b) are plotted to depict the alteration in magnitude of the velocity profile $\bar{F}'(\bar{\chi},\bar{\tau})$ due to the stimulus of the couple stress parameter (λ), solid volume fraction constant (φ), radius of curvature variable (C_1), and magnetic constant (M) on the velocity profile when $\bar{\tau}=8.5\pi$ and $\bar{\tau}=9.5\pi$. From the graphical trends, it is remarked that at $\bar{\tau}=8.5\pi$, the velocity field $\bar{F}'(\bar{\chi},\bar{\tau})$ exhibits a declining fashion against growing values of all the aforementioned variables (see Figures 4(a), 5(a), 6(a), 7(a)). In contrast at $\bar{\tau}=9.5\pi$, the velocity profile $\bar{F}'(\bar{\chi},\bar{\tau})$ shows a progressive enhancement as the magnitudes of these parameters increase (see Figures 4(b), 5(b), 6(b), 7(b)).

Figures 8(a) and 8(b) reveal the impressions of diverse time intervals $\bar{\tau}=3\pi/2,\ \pi,\pi/2$ and $\bar{\tau}=\pi/2,\pi/3,\pi/4,\pi/6$ on the profile of velocity $\bar{F}'(\bar{\chi},\bar{\tau})$. Figure 8(a) clarifies that the limit of $\bar{F}'(\bar{\chi},\bar{\tau})$ remains confined within the range (–1 to 1), which can be attributed to the oscillatory nature of the surface. The imposed oscillations periodically accelerate and decelerate the fluid motion, thereby restricting the velocity amplitude within this bounded interval. In converse, Figure 8(b) shows that $\bar{F}'(\bar{\chi},\bar{\tau})$ grows with uplifting values of $\bar{\tau}$. This trend implies that as $\bar{\tau}$ grows, the continued oscillations of the surface continuously impart energy and momentum to the adjacent fluid layers. Over time, these oscillations accumulate their influence, resulting in a strengthening of the fluid motion rather than its decay. Consequently, the velocity profile exhibits a noticeable enhancement at larger values of $\bar{\tau}$, emphasizing the role of oscillatory forcing in accelerating the flow. Such behavior is highly relevant in practical systems where oscillatory boundary conditions are common, for instance, in pulsatile blood flow, oscillating cooling channels in thermal management devices, and vibration-driven transport in industrial processes.

The influences of parameters (λ), (φ), (C_1), and unsteady variable (S) on the pressure field $\bar{P}(\bar{\chi},\bar{\tau})$ are described via Figure 9(a-d), respectively. The pressure amplitude shows the contrary manner against higher values of (C_1) and (λ), whilst with improving values of (φ) and (S), the pressure amplitude develops. Physically, an increase in (φ) enhances the effective density and viscosity of the nanofluid, thereby fortifying fluid–particle interactions and elevating the pressure gradient. On the other hand, the unsteady parameter, which is the ratio of oscillation frequency to the stretching rate of the surface, reflects the dominance of oscillatory motion over stretching effects. Larger values of the unsteady parameter signify stronger oscillatory forcing, which amplifies the temporal variations in the flow and leads to higher pressure fluctuations. These features are mainly relevant in oscillatory nanofluid transport, pulsatile biomedical flows and industrial processes involving vibration-assisted fluid motion, where controlling pressure fluctuations is critical for efficiency and stability.

Figure 10(a-d) is plotted to depict the variations in the magnitude of the pressure field $\bar{P}(\bar{\chi},\bar{\tau})$ under the consequences of (λ), (φ), (C_1), and (M) when $\bar{\tau}=0.5\pi$ fixed. The graphical results demonstrate a converse trend of pressure field against all the above-defined parameters.

Figure 11(a-f) displays the significance of the Dufour number (D_u), solid volume fraction parameter (φ), ratio parameter (γ), thermophoretic variable (N_t), Brownian constant (N_b), radiation variable (R_d), Prandtl number (P_r), and radius of curvature parameter (C_1) on $\bar{\Theta}(\bar{\chi},\bar{\tau})$ at $\bar{\tau}=0.5\pi$. It is confirmed that the temperature profile $\bar{\Theta}(\bar{\chi},\bar{\tau})$ is enhanced for varying values of (C_1), (R_d), (D_u), and (φ). While the temperature profile $\bar{\Theta}(\bar{\chi},\bar{\tau})$ shows a contrary response with advanced values of (N_t), (P_r), (γ), and (N_b). The enhancement in the temperature profile with the Dufour number arises from the cross-diffusion effect, where concentration gradients generate an additional energy flux in the energy equation, thereby intensifying the thermal transport mechanism. Whereas, the reduction in the temperature profile with increasing Prandtl number occurs because the Prandtl number represents the ratio of momentum diffusivity to thermal diffusivity. Higher values of Prandtl number correspond to weaker thermal diffusivity, which diminishes heat transfer, thins the thermal boundary layer, and consequently lowers the fluid temperature. These mechanisms are of practical significance in chemical and combustion systems, geophysical flows, nanofluid-based cooling devices and thermal system design, where cross-diffusion and thermal boundary layer control play a vital role in optimizing heat and mass transport.

The variation in the concentration distribution $\bar{\Phi}(\bar{\chi},\bar{\tau})$ due to the stimuli of diverse parameters, namely Soret number (S_r), thermophoretic variable (N_t), Lewis number (L_e), and Brownian parameter (N_b) is presented via Figure 12(a-d). From graphical outcomes, it is noted that the nanoparticle concentration field exhibits a mounting trend behavior with improving values of (S_r). Larger values of the Soret number enhance the thermally induced mass flux, which strengthens solutal transport and enlarges the concentration field and concentration boundary layer thickness. In contrast, the concentration profile drops against the other above-mentioned variables. The reduction in concentration with the thermophoretic variable occurs because thermophoresis drives nanoparticles away from the heated wall toward the colder bulk fluid region, thereby reducing near-wall concentration. Similarly, higher Brownian motion intensifies random nanoparticle diffusion, which weakens local concentration gradients and diminishes the concentration distribution. These effects hold significant importance in natural and engineering systems such as geophysical mass transfer, in separation processes and combustion systems, where the balance between thermal and solutal diffusion directly governs performance and efficiency.

Figures 13(a) and 14(a) illustrate the behavior of the streamlines corresponding to the axial velocity component $\bar{w}_1(\bar{x}_1,\bar{t})$ and the radial velocity component $\bar{w}_2(\bar{x}_2,\bar{t})$ for $\bar{\tau}\in(0,10\pi)$. Both graphs exhibit the oscillatory nature of the streamlines.

Figures 13(b), 14(b), and 15(a-b) demonstrate the behavior of streamlines of the radial velocity component $\bar{w}_2(\bar{x}_2,\bar{t})$ and axial velocity component $\bar{w}_1(\bar{x}_1,\bar{t})$, isotherms, and isoconcentration contours when $\bar{\tau}=0.5\pi$ fixed. These graphs highlight the symmetrical response of the streamlines, isotherms, and isoconcentration contours.

Figure 16(a-d) interpreted the influences of governing flow parameters, such as the couple stress parameter (λ), solid volume fraction variable (φ), unsteady parameter (S), and radius of curvature parameter (C_1) on the skin friction coefficient $\bar{C}_{\bar{F}}\left(\sqrt{\mathrm{Re}_s}\right)$ for $\bar{\tau}\in(0,10\pi)$. It is clearly seen from this graph that the amplitude of the skin friction profile $\bar{C}_{\bar{F}}\left(\sqrt{\mathrm{Re}_s}\right)$ is reduced with (C_1) and is enlarged with uplifting (λ), (S), and (φ).

Figure 17(a) and 17(b) illustrate the alteration in the magnitude of the skin friction coefficient $\bar{C}_{\bar{F}}\left(\sqrt{\mathrm{Re}_s}\right)$ due to the effects of the couple stress parameter (λ) versus solid volume fraction variable (φ), and magnetic parameter (M) versus radius of curvature parameter (C_1) when $\bar{\tau}=0.5\pi$. This graph clarifies that skin friction magnitude $\bar{C}_{\bar{F}}\left(\sqrt{\mathrm{Re}_s}\right)$ improves with increasing values of the couple stress parameter (λ), solid volume fraction variable (φ), and the magnetic parameter, and it depicts a contrary response against the radius of curvature parameter (C_1).

Table 2 emphasizes the effects of the Dufour number (D_u), solid volume fraction parameter (φ), ratio parameter (γ), thermophoretic variable (N_t), Brownian constant (N_b), radiation variable (R_d), Prandtl number (P_r), and radius of curvature parameter (C_1) on the numerical magnitude of the local Nusselt number $\left(Nu_s/\sqrt{\mathrm{Re}_s}\right)$. This table argues that with enlarged values of (R_d), (N_t), (γ), (N_b), and (φ) the absolute values of the Nusselt number $\left(Nu_s/\sqrt{\mathrm{Re}_s}\right)$ show a growing trend. However, a contrary response is remarked with elevated values of (D_u), (C_1), and (P_r). Table 3 reveals that the magnitude of the local Sherwood number $\left(Sh_s/\sqrt{Re_s}\right)$ intensifies with varying values of the Lewis number and Brownian parameter. An increment in the Lewis number reduces mass diffusivity, resulting in a sharper concentration gradient at the wall and enhanced mass transfer. Similarly, stronger Brownian motion promotes nanoparticle diffusion near the surface, leading to an increased mass flux. In contrast, the local Sherwood number $\left(Sh_s/\sqrt{Re_s}\right)$ magnitude declines with thermophoretic

variable, radius of curvature, and Soret number. The physical reason for the decrease in the local Sherwood number $\left(Sh_s / \sqrt{Re_s}\right)$ magnitude with higher values of the thermophoretic parameter and Soret number is that the stronger thermophoretic effects drive nanoparticles away from the heated surface, thickening the concentration boundary layer and reducing the wall concentration gradient, while higher Soret numbers promote thermally induced diffusion, which weakens the surface concentration gradient and further decreases the Sherwood number $\left(Sh_s / \sqrt{Re_s}\right)$.

Table 4 is presented to validate the obtained results of $\bar{f}''(0,\bar{\tau})$ by comparison with existing literature [5, 23] in a limiting case. The table witnesses that the current outcomes are in good agreement with the published solutions, confirming the accuracy of the present analysis.

5. Conclusions

The current novel analysis examines the combined effects of Soret and Dufour phenomena, thermophoresis, Brownian diffusion and impacts of nonlinear thermal radiation in an alumina–water couple stress nanofluid on a curved oscillatory stretching surface. The formulated partial differential equations are solved analytically by incorporating the homotopy analysis method (HAM). The important findings of this study are summarized as follows:

- Velocity amplitude depicts a contrary trend with escalation of the couple stress parameter, solid volume fraction, radius of curvature, and magnetic parameter, indicating enhanced flow resistance due to microstructural, magnetic and geometric effects. This observation is valuable for controlling flow strength in an oscillatory and magnetically controlled nanofluid systems such as cooling channels, magneto-hydrodynamic pumps, lubrication devices and vibration assisted transport processes.
- At $\bar{\tau} = 8.5\pi$, the velocity field declines against the magnetic and couple stress parameters, radius of curvature and solid volume fraction signifying dominant resistive effects through the deceleration phase of oscillation. However, at $\bar{\tau} = 9.5\pi$, the velocity field shows an improved response to the same parameters, reflecting phase dependent acceleration induced by the oscillatory stretching surface. This phenomenon highlights the importance of the oscillation phase in regulating flow dynamics in unsteady nanofluid transport systems which includes in vibration driven transport processes, pulsatile pumping, oscillatory cooling channels and biomedical flows where time dependent flow control is critical.
- Velocity of the fluid is improved with changing instants of time $\bar{\tau} = \pi/2, \pi/3, \pi/4, \pi/6$. This rising response of the velocity reflects that the time dependent acceleration induced by the oscillatory stretching surface representing the importance of phase dependent flow control in unsteady nanofluid transport, such as oscillating cooling channels, pulsatile blood flow, microfluidic pumping systems and vibration assisted transport processes.

- Amplitude of the fluid pressure distribution is a growing function of the unsteady parameter and solid volume fraction. Though, with rising values of the radius of curvature and couple stress parameter, the amplitude of the pressure distribution declines. These mechanisms highlight the role of surface geometry and fluid microstructure in controlling pressure oscillations in unsteady transport processes such as oscillatory microfluidic devices, peristaltic transport and pulsatile pumping systems.
- Temperature distribution increases with an increase in the Dufour number, radius of curvature, radiation parameter and solid volume fraction parameter. While, it decreases with higher values of the Brownian parameter, temperature ratio parameter, thermophoretic parameter and Prandtl number. This behavior highlights the importance of coupled thermal–mass diffusion mechanisms and radiative effects in regulating thermal boundary layers in nanofluid systems particularly in the fields of thermal energy storage devices, cooling technologies, microfluidic systems and industrial heat transfer applications.
- Magnitude of concentration distribution shows a promising response with higher values of the Soret number. Whilst, it decreases gradually for rising values of Brownian and thermophoresis parameters and Lewis number showing the competing impacts of nanoparticle migration and thermal diffusion in mass transport. These mechanisms are mostly relevant in engineering and natural systems, such as nanofluid-based cooling devices, combustion systems, separation processes and geophysical mass transfer where the interaction between solutal and thermal diffusions governs transport efficiency and overall performance.
- Amplitude of skin friction raises with varying values of the solid volume fraction, couple stress parameter and unsteady parameter reflecting increased wall shear due to increase in fluid resistance and nanoparticle loading. This finding is significant for predicting mechanical stresses and surface drag in oscillatory nanofluid flows.
- Numerical magnitude of the heat transmission rate rises with increasing radiation parameter, thermophoresis and Brownian diffusions, solid volume fraction parameter, and temperature ratio parameter. Though, it declines with developed values of the radius of curvature and Dufour number. For instance, it is noticed that growing the Dufour number from 0 to 1 decreases the Nusselt number by approximately 1.4%, indicating a mild weakening of surface heat transfer due to cross diffusion effects. Also, the radius of curvature parameter considerably suppresses the heat transfer rate as by increasing the radius of curvature from 1.0 to 5.0 leads to an approximate 50% decline in the Nusselt number. These trends offer guidance for optimizing thermal performance in nanofluid-based heat transfer systems, particularly in micro- and macro-scale cooling devices, industrial process equipment, heat exchangers and thermal energy storage units.
- Numerical magnitude of the local Sherwood number displays a declining manner with growing radius of curvature, Soret number and thermophoresis parameter. However, for increasing Brownian parameter and Lewis number, it is improved. From the tabulated data, it is noticed that growing the Lewis number from 0.5 to 1.5 increases the Sherwood number magnitude by approximately 9%, representing stronger

nanoparticle mass transfer due to reduced mass diffusivity. This behavior highlights the understanding of mass transfer rates to cross diffusion effects, nanoparticle motion and surface geometry in coupled transport processes, including separation and purification systems, chemical reactors and microfluidic applications.

The main outcomes of the current study can be extended toward physical industrial and engineering applications by adding more realistic physical effects. Future study may consider hybrid or ternary hybrid nanofluids with Brownian and thermophoresis diffusions, along with temperature dependent thermophysical properties to enhance thermal systems in high performance heat exchangers, thermal energy storage devices, biomedical applications and cooling systems. The incorporation of velocity and thermal slip boundary conditions, melting heat transfer, viscous dissipation, Joule heating and homogeneous–heterogeneous chemical reactions would further improve the applicability of the model to metallurgical operations, coating processes, microfluidic devices and polymer extrusion. Furthermore, applying data-driven or numerical approaches such as finite element simulations can help to design optimization and real time control strategies in advanced industrial and engineering heat and mass transfer systems.

Data availability statement

The datasets used and/or analysed during the current study available from the corresponding author on reasonable request.

Declaration of conflicting interests

The author(s) declared no potential conflicts of interest with respect to the research, authorship, and/or publication of this article.

Funding statement

The author(s) received no financial support for the research, authorship, and/or publication of this article.

Ethical approval

This study does not involve human participants, animals, or any sensitive data requiring ethical approval.

Informed consent

There are no human participants in this article and informed consent is not required.

References

[1] Choi, S.U.S., “Enhancing thermal conductivity of fluids with nanoparticle”, In ASME International Mechanical Engineering Congress and Exposition, American Society of Mechanical Engineers, **17421**, pp. 99-105 (1995). https://doi.org/10.1115/IMECE1995-0926

[2] Ragulkumar, E., Palani, G., Sambath, P., et al. “Dissipative MHD free convective nanofluid flow past a vertical cone under radiative chemical reaction with mass flux” Scientific Reports, **13**(1), pp. 2878 (2023). https://doi.org/10.1038/s41598-023-28702-0

[3] Imran, M., Naveed, M., Iftikhar, B., et al. “Heat transfer analysis in a curvilinear flow of hybrid nanoliquid across a curved oscillatory stretched surface with nonlinear thermal radiation”, ZAMM-Journal of Applied Mathematics and Mechanics/Zeitschrift für Angewandte Mathematik und Mechanik, **103**(11), pp. e202200600 (2023). https://doi.org/10.1002/zamm.202200600

[4] Mohana, C. M., Kumar, B. R., “Nanoparticle shape effects on MHD Cu–water nanofluid flow over a stretching sheet with thermal radiation and heat source/sink”, International Journal of Modern Physics B, **38**(10), pp. 2450151 (2024). https://doi.org/10.1142/S0217979224501510

[5] Naveed, M., Imran, M., Abbas, Z., “Effect of chemical reaction on bioconvective flow of gyrotactic micro-organisms in hybrid nanofluid on a curved oscillating surface with thermal radiation”, Arabian Journal for Science and Engineering, **50**, pp. 20543–20562 (2025). https://doi.org/10.1007/s13369-025-10131-y

[6] Syam, M. M., Alkhedher, M., Syam, M. I., “Thermal and hydrodynamic analysis of MHD nanofluid flow over a permeable stretching surface in porous media: Comparative study of Fe3O4, Cu, and Ag nanofluids”, International Journal of Thermofluids, **26**, pp. 101055 (2025). https://doi.org/10.1016/j.ijft.2025.101055

[7] Buongiorno, J., Convective transport in nanofluids. pp. 240-250 (2006). https://doi.org/10.1115/1.2150834

[8] Ahmed, K., Akbar, T., Muhammad, T., et al. “Heat transfer characteristics of MHD flow of Williamson nanofluid over an exponential permeable stretching curved surface with variable thermal conductivity”, Case Studies in Thermal Engineering, **28**, pp.101544 (2021). https://doi.org/10.1016/j.csite.2021.101544

[9] Imran M., Naveed, M., “Analysis of thermophoretic and Brownian diffusions in hydromagnetic curvilinear flow of Carreau nanofluid with activation energy and heat generation”, Results in Engineering, **24**, pp. 103114 (2024). https://doi.org/10.1016/j.rineng.2024.103114

[10] Ali, A., Ali, M., Hussain, M., et al. “The influence of thermophoresis and Brownian motion on maxwell nanofluids utilizing Cattaneo-Christov double diffusion theory”, Advances in Mechanical Engineering, **16**(11), pp. 16878132241302999 (2024). https://doi.org/10.1177/16878132241302999

[11] Sankaralingam, K., Damodharan, I., Albidah, A. B., et al. “Heat and mass transfer analysis on magnetohydrodynamics Powell–Eyring nanofluid flow with Hall current, thermal radiation, Brownian motion, and thermophoresis effects over a stretched surface”, ZAMM-Journal of Applied Mathematics and Mechanics/Zeitschrift für Angewandte Mathematik und Mechanik, **105**(1), pp. e202300900 (2025). https://doi.org/10.1002/zamm.202300900

[12] Majidi Zar, P., Shateri, A., Jalili, P., et al. “Radiative effects on 2D unsteady MHD Al2O3-water nanofluid flow between squeezing plates: A comparative study using AGM and HPM in Python”, ZAMM-Journal of Applied Mathematics and Mechanics/Zeitschrift für Angewandte Mathematik und Mechanik, **105**(2), pp. e202400546, (2025). https://doi.org/10.1002/zamm.202400546

[13] Shateri, A., Moghaddam, M. M., Jalili, B., et al. “Heat transfer analysis of unsteady nanofluid flow between moving parallel plates with magnetic field: analytical approach”,. Journal of Central South University, **30**(7), pp. 2313-2323 (2023). https://doi.org/10.1007/s11771-023-5388-3

[14] Mishra, S., Mondal, H., Kundu, P. K., “Dynamics of magneto-bioconvection thermal casson nanofluid with activation energy and joule heating”, Numerical Heat Transfer, Part B: Fundamentals, **86**(11), pp. 3854-3882 (2025). https://doi.org/10.1080/10407790.2024.2367701

[15] Sarkar, A., Mondal, H., Nandkeolyar, R., “Impact of chemical reaction on magnetohydrodynamics non-Darcian mixed convective nanofluid flow past over a stretching sheet with non-uniform heat source/sink”, Scientia Iranica. Transaction B, Mechanical Engineering, 32(6), pp. 1-15 (2025). https://doi.org/10.24200/sci.2024.60844.7017

[16] Mishra, S., Mondal, H., Kundu, P. K., “Analysis of activation energy and microbial activity on couple stress nanofluid with heat generation”, International Journal of Ambient Energy, **45**(1), pp. 2266429 (2024). https://doi.org/10.1080/01430750.2023.2266429

[17] Mishra, S., Mondal, H., Kundu, P. K., “Entropy optimisation of a viscous bioconvective nanofluid flow with Coriolis and Lorentz forces using bivariate spectral quasi-linearisation technique”, Pramana, **99**(1), pp. 11 (2024). https://doi.org/10.1007/s12043-024-02855-7

[18] Mishra, S., Mondal, H., “A neuro-computational proposal for the ZrO2-Fe3O4 nanoparticles in the engine oil–based hybrid nanofluid: BioNanoScience, 14(5), pp. 4985-5002 (2024). https://doi.org/10.1007/s12668-023-01282-z

[19] Stokes, V. K., “Couple stresses in fluids”, Physics of Fluids, **9**(9), pp. 1709-1715 (1966). https://doi.org/10.1063/1.1761925

[20] Alabdan, R., Khan, S. U., Al-Qawasmi, A.R., et al. “Applications of temperature dependent viscosity for Cattaneo–Christov bioconvection flow of couple stress nanofluid over oscillatory stretching surface: a generalized thermal model”, Case Studies in Thermal Engineering, **28**, pp. 101412 (2021). https://doi.org/10.1016/j.csite.2021.101412

[21] Mahesh, R., Mahabaleshwar, U. S., Kumar, P. V., et al. “Impact of radiation on the MHD couple stress hybrid nanofluid flow over a porous sheet with viscous dissipation”, Results in Engineering, **17**, pp. 100905 (2023). https://doi.org/10.1016/j.rineng.2023.100905

[22] Naveed, M., Imran, M., Gul, S., “Heat transfer analysis in hydromagnetic flow of couple stress fluid in presence of homogeneous and heterogeneous chemical reactions over a porous oscillatory stretchable sheet”, Advances in Mechanical Engineering, **15**(2), pp. 16878132231155823 (2023). https://doi.org/10.1177/16878132231155823

[23] Imran, M., Naveed, M., Abbas, Z., "Dynamics of Soret and Dufour effects on oscillatory flow of couple stress fluid due to stretchable curved surface", Advances in Mechanical Engineering, **15**(2), pp. 16878132231156742 (2023). https://doi.org/10.1177/16878132231155823

[24] Zhang, L., Bhatti, M. M., Michaelides, E. E., et al. "Characterizing quadratic convection and electromagnetically induced flow of couple stress fluids in microchannels", Qualitative theory of dynamical systems, **23**(1), pp. 35 (2024). https://doi.org/10.1007/s12346-023-00883-z

[25] Umavathi, J. C., Buonomo, B., Manca, O., et al. "MHD Couple Stress boundary-layer flow with heat and mass transfer under thermal radiation and Marangoni effect: A Numerical study", Case Studies in Thermal Engineering, pp. 106159 (2025). https://doi.org/10.1016/j.csite.2025.106159

[26] Shabbir, T., Mushtaq, M., Khan, M. I., et al. "Modeling and numerical simulation of micropolar fluid over a curved surface: Keller box method", Computer methods and programs in biomedicine, **187**, pp. 105220 (2020). https://doi.org/10.1016/j.cmpb.2019.105220

[27] Qian, W. M., Khan, M. I., Shah, F., Mathematical modeling and MHD flow of micropolar fluid toward an exponential curved surface: heat analysis via ohmic heating and heat source/sink", Arabian Journal for Science and Engineering, **47**(1), pp. 867-878 (2022). https://doi.org/10.1007/s13369-021-05673-w

[28] Jalili, B., Ganji, A. M., Shateri, A., et al. "Thermal analysis of non-Newtonian visco-inelastic fluid MHD flow between rotating disks", Case Studies in Thermal Engineering, **49**, pp. 103333 (2023). https://doi.org/10.1016/j.csite.2023.103333

[29] Mahboobtosi, M., Jalili, B., Shateri, A., et al. "Heat transfer characteristics in the squeezing flow of casson fluid between circular plates: A comprehensive study", Advances in Mechanical Engineering, **16**(10), pp. 16878132241290942 (2024). https://doi.org/10.1177/16878132241290942

[30] Dinesh, P., Yadav, S., Jyothirmayi, M., "Nonlinear stretching curved surface and Lorentz force effect on hybrid nanofluids with an activation energy", International Journal of Thermofluids, **24**, pp. 100983 (2024). https://doi.org/10.1016/j.ijft.2024.100983

[31] Haq, S. U., Ashraf, M. B., Nawaz, R., "MHD flow of Carreau fluid over a curved stretching surface with Cattaneo–Christov heat flux model and chemical reaction", Numerical Heat Transfer, Part B: Fundamentals, **86**(6), pp. 1583-1598 (2025). https://doi.org/10.1080/10407790.2024.2317922

[32] Imran, M., Naveed, M., Rasheed, M. W., "Analysis of heat transfer in magnetized Williamson fluid over a porous curved oscillating surface: Entropy generation", International Journal of Geometric Methods in Modern Physics, **22**(11), pp. 2550087 (2025). https://doi.org/10.1142/S0219887825500872

[33] Naveed, M., Imran, M., Asghar, T., et al. "Transport mechanism in chemically reactive hybrid nanofluid flow containing gyrotactic micro-organisms over a curved oscillatory

surface", Applied Mathematics and Mechanics (English Edition), **46**(1), pp.177-192 (2025). https://doi.org/10.1007/s10483-025-3208-7

[34] Naveed, M., Imran, M., Khadim, F., "Dynamics of chemical reactions and temperature-dependent thermal conductivity in a viscous fluid over an oscillating curved surface", Science Progress, **108**(2), pp. 00368504251343498 (2025). https://doi.org/10.1177/00368504251343498

[35] Almakki, M., Mondal, H., Mishra, S., "Study of viscosity variation and inconsistency of non-Newtonian fluid flow over oscillating surface", International Journal of Heat and Fluid Flow, **117**, 110131 (2026). https://doi.org/10.1016/j.ijheatfluidflow.2025.110131

[36] Shilpa, B., Leela, V., Prasannakumara, B. C., et al. "Soret and Dufour effects on MHD double-diffusive mixed convective heat and mass transfer of couple stress fluid in a channel formed by electrically conducting and non-conducting walls", Waves in Random and Complex Media, **35**(6), pp. 10980-11001 (2022). https://doi.org/10.1080/17455030.2022.2119491

[37] Islam, A., Mahmood, Z., Khan, U., et al. "Lie scaling transformations for the analysis of MHD flow with radiation, Soret, and Dufour effects as well as viscous dissipation across a convective surface during triple diffusion", International Journal of Heat and Fluid Flow, **108**, pp. 109465 (2024). https://doi.org/10.1016/j.ijheatfluidflow.2024.109465

[38] Farooq, U., Liu, T., Farooq, U., et al. "Non-similar analysis of bioconvection MHD micropolar nanofluid on a stretching sheet with the influences of Soret and Dufour effects", Applied Water Science, **14**(6), pp. 116 (2024). https://doi.org/10.1007/s13201-024-02143-0

[39] Nagari, H. C., Firdi, M. D., Rikitu, E. H., "Analyzing Soret and Dufour effects on MHD variable viscosity Casson nanofluid flow past a stretching sheet with heat source/sink", Advances in Mathematical Physics, **2025**(1), pp. 2167629 (2025). https://doi.org/10.1155/admp/2167629

[40] Reddy, B. A. P., "A study of irreversibility on nonlinear thermal radiation and MHD flow of Casson and Carreau ternary hybrid nanofluid over a vertical porous plate", Numerical and statistical approach. Numerical Heat Transfer, Part A: Applications, pp. 1–35 (2024). https://doi.org/10.1080/10407782.2024.2311765

[41] Sulochana, C., Nandeppanavar, A. L., Nandeppanavar, M. M., et al. "Effect of activation energy and nonlinear thermal radiation on flow, heat and mass transfer of magneto-bioconvective Eyring–Powell nanofluid due to a stretching sheet", Proceedings of the Institution of Mechanical Engineers, Part N: Journal of Nanomaterials, Nanoengineering and Nanosystems, pp. 23977914251330675 (2024). https://doi.org/10.1177/23977914251330675

[42] Anjum, A., Maheswari, C., Lakshmi, B. N., et al. "Computational study of magnetized 3D revolving hybrid nanofluid with non-linear thermal radiation and heat source/sink over a stretching sheet", Multiscale and Multidisciplinary Modeling, Experiments and Design, **8**(3), pp. 200 (2025). https://doi.org/10.1007/s41939-025-00748-9

[43] Ganji, D. D., Mahboobtosi, M., Chari, F. N., "Nonlinear radiation in entropy generation MHD flow of penta-hybrid nanofluids: Effects of variable thermal conductivity, viscous

dissipation and nonlinear convection", Journal of Radiation Research and Applied Sciences, **18**(2), pp. 101524 (2025). https://doi.org/10.1016/j.jrras.2025.101524

Biographies

Dr. Muhammad Naveed is working as an Associate Professor in the Department of Mathematics, University of Education, Lahore. He earned Ph.D. degree in Applied Mathematics. His research interests include Newtonian and non-Newtonian fluid flow, Magnetohydrodynamics (MHD), Fluid Flow in Porous Medium, Heat and Mass Transfer, Nanofluid flow, flow on various shapes of curved geometries, and Analytical and Numerical Solutions for ODEs and PDEs.

Dr. Muhammad Imran is serving as an Assistant Professor at the University of Education, Lahore, Pakistan. He obtained his Ph.D. degree in Applied Mathematics. His primary research interest is in Fluid Mechanics, Heat and Mass Transfer analysis, nanofluid flow, Flow analysis on curved oscillatory geometries, and Analytical and Numerical computations for ODEs and PDEs.

Mr. Waqas Ahmad has completed his M.S. in Mathematics from the University of Education, Lahore, Pakistan. His research interests include nanofluids, non-Newtonian fluids over a curved oscillatory surface, and heat and mass transfer.

Figure 1: Flow Geometry

Figure 2: Flow chart illustrating the Homotopy Analysis Method (HAM).

Figure 3: Deviation in velocity field $\bar{F}'(\bar{\chi},\bar{\tau})$ when $\bar{\tau}=(0,10\pi)$.

Figure 4: Effects of λ on $\bar{F}'(\bar{\chi},\bar{\tau})$.

Figure 5: Effects of φ on $\bar{F}'(\bar{\chi},\bar{\tau})$.

Figure 6: Effects of C_1 on $\bar{F}'(\bar{\chi},\bar{\tau})$.

Figure 7: Effects of M on $\bar{F}'(\bar{\chi},\bar{\tau})$.

Figure 8: Effects of $\bar{\tau}$ on $\bar{F}'(\bar{\chi},\bar{\tau})$.

Figure 9: Alteration in pressure profile $\bar{P}(\bar{\chi},\bar{\tau})$.

Figure 10: Alteration in pressure profile $\bar{P}(\bar{\chi},\bar{\tau})$.

Figure 11: Deviation in temperature profile $\bar{\Theta}(\bar{\chi},0.5\pi)$.

Figure 12: Deviation in concentration profile $\bar{\Phi}(\bar{\chi},0.5\pi)$

Figure 13: Variations in Streamlines of axial velocity component $\bar{w}_1(\bar{x}_1,\bar{t})$.

Figure 14: Variations in Streamlines of normal velocity component $\bar{w}_2(\bar{x}_2,\bar{t})$.

Figure 15: Variations in Isotherms and Isoconcentration contours when $\bar{\tau}=0.5\pi$.

Figure 16: Variation in skin friction coefficient $\left(\bar{C}_{\bar{F}}\left(\sqrt{\mathrm{Re}_s}\right)\right)$.

Figure 17: Alteration in skin friction coefficient $\left(\bar{C}_{\bar{F}}\left(\sqrt{\mathrm{Re}_s}\right)\right)$ when $\bar{\tau}=0.5\pi$.

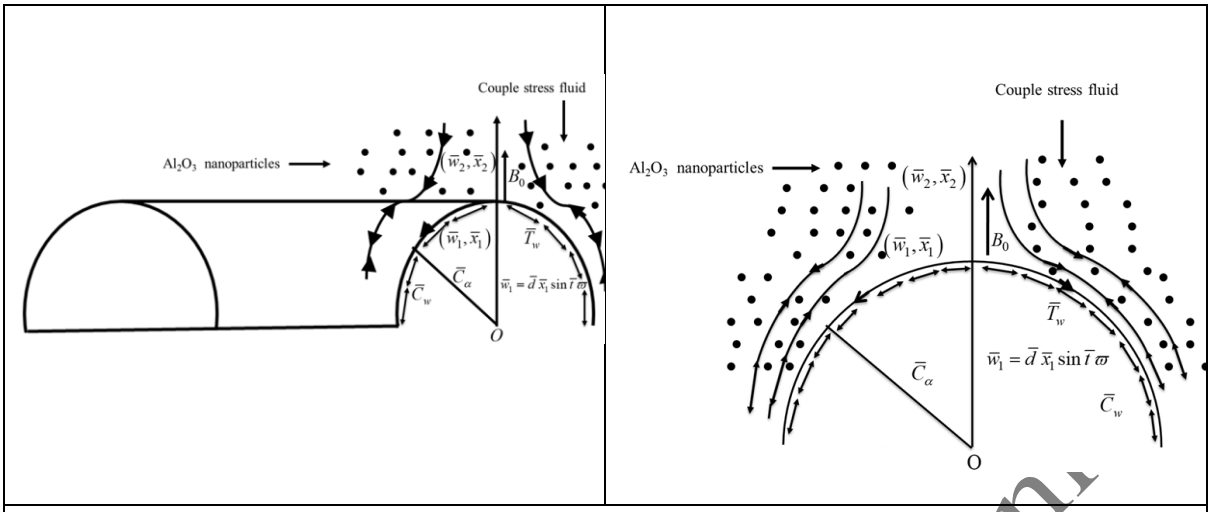

Figure 1: Flow Geometry

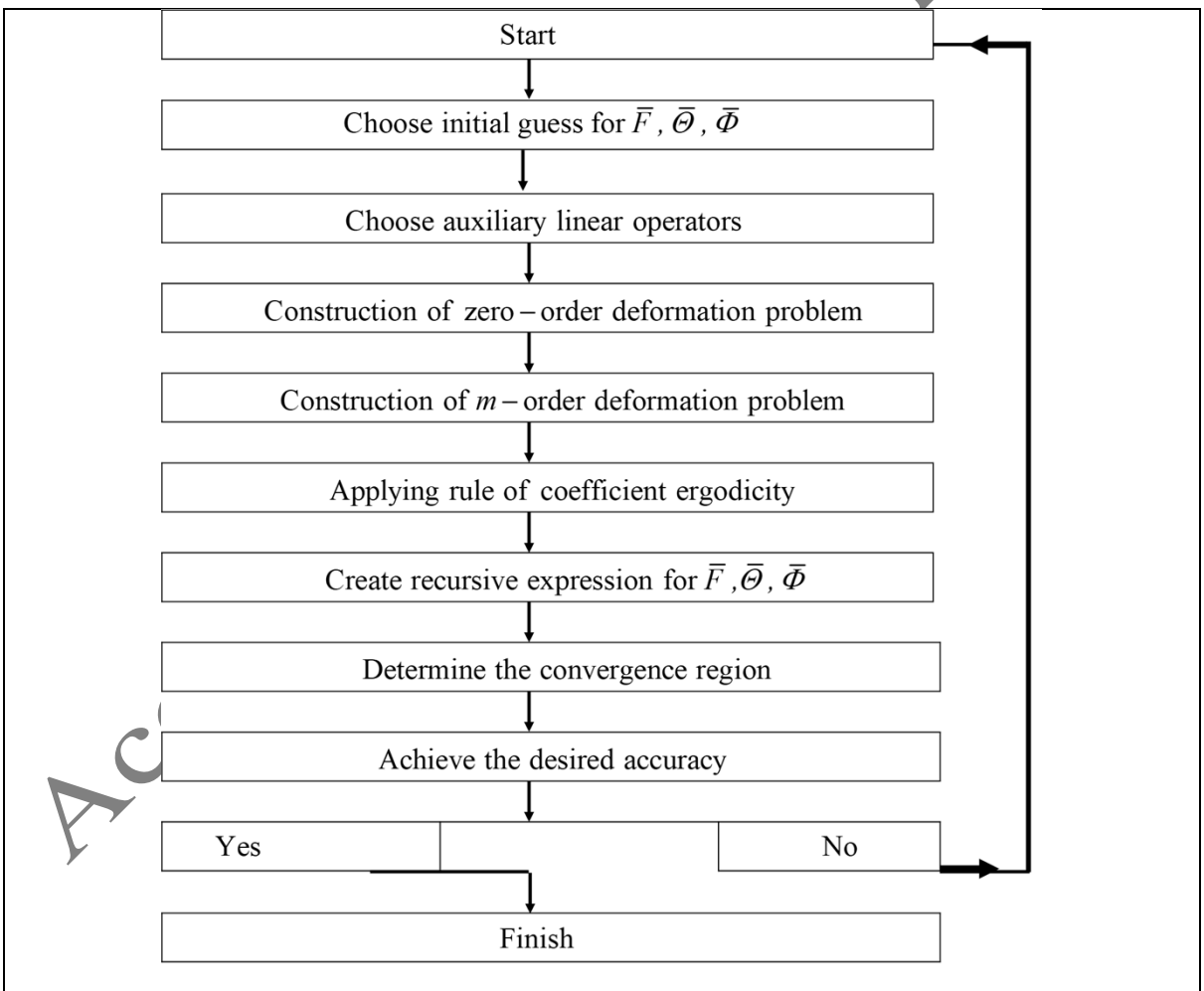

Figure 2: Flow chart illustrating the Homotopy Analysis Method (HAM).

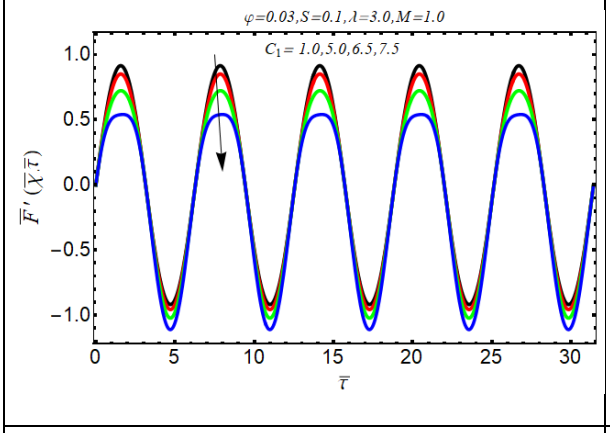

(a)

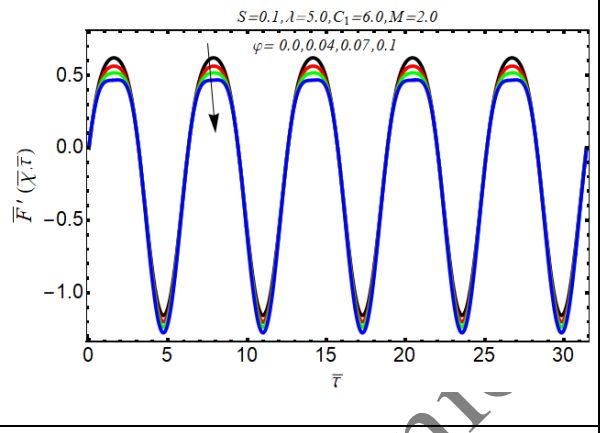

(b)

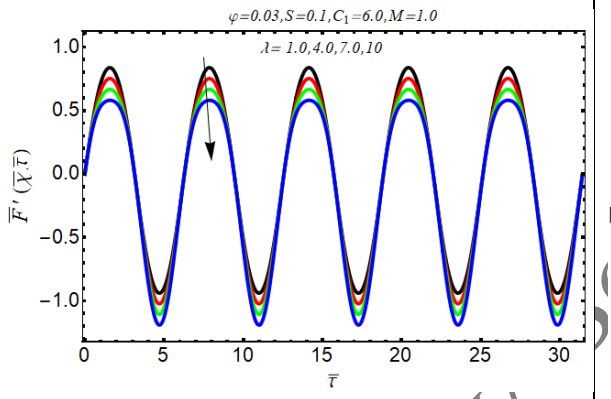

(c)

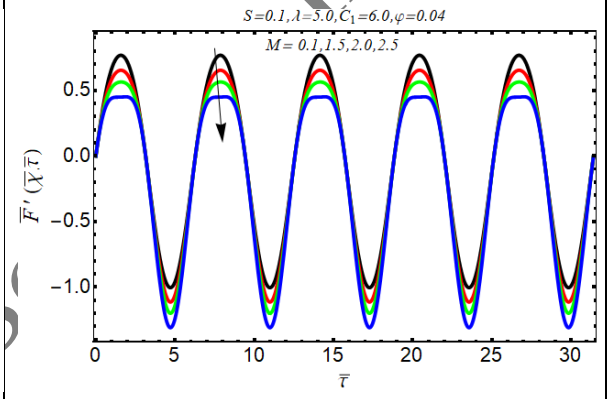

(d)

Figure 3: Deviation in velocity field $\bar{F}'(\bar{\chi},\bar{\tau})$ when $\bar{\tau}=(0,10\pi)$.

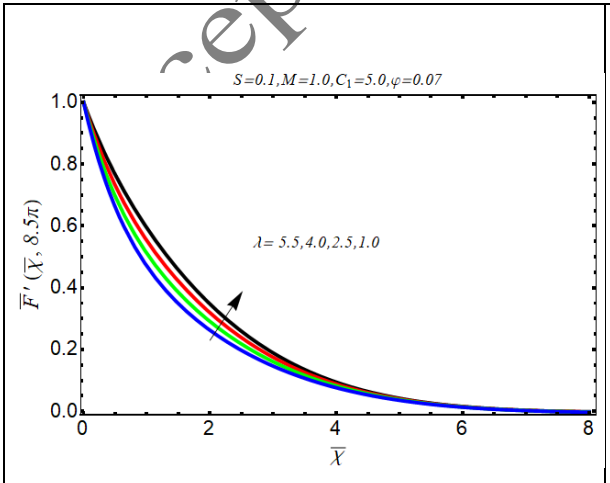

(a)

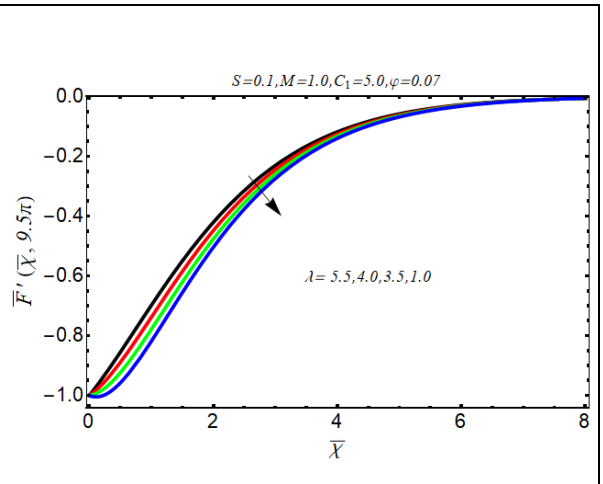

(b)

Figure 4: Effects of λ on $\bar{F}'(\bar{\chi},\bar{\tau})$.

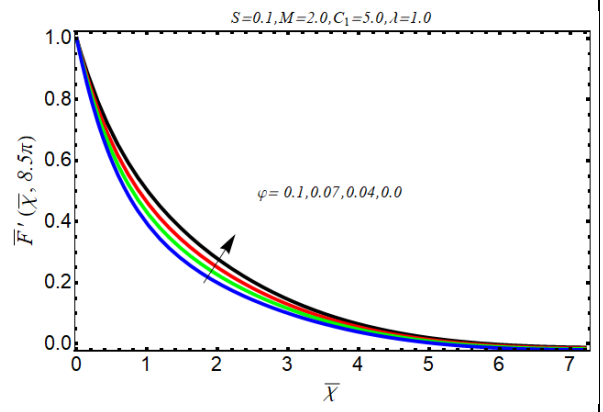

(a)

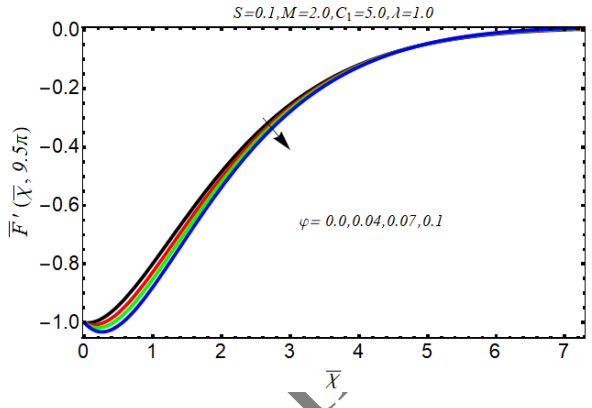

(b)

Figure 5: Effects of φ on $\bar{F}'(\bar{\chi},\bar{\tau})$.

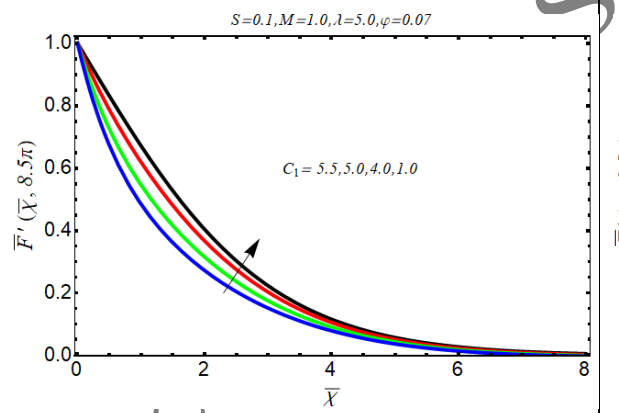

(a)

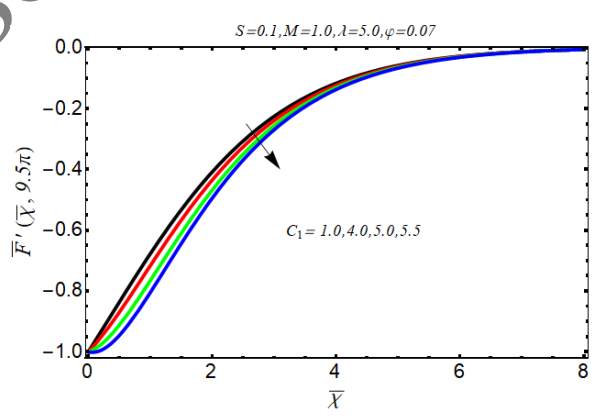

(b)

Figure 6: Effects of C_1 on $\bar{F}'(\bar{\chi},\bar{\tau})$.

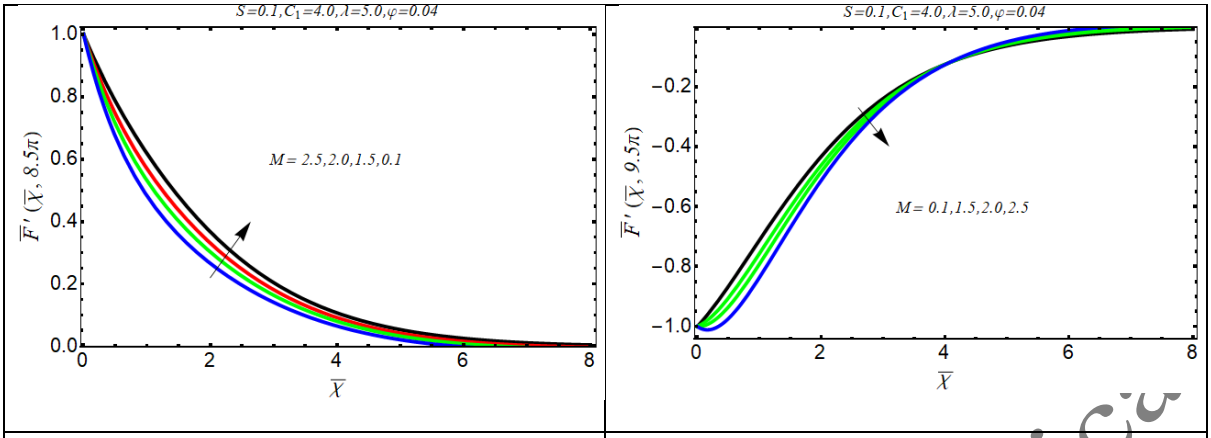

(a) (b)

Figure 7: Effects of M on $\bar{F}'(\bar{\chi},\bar{\tau})$.

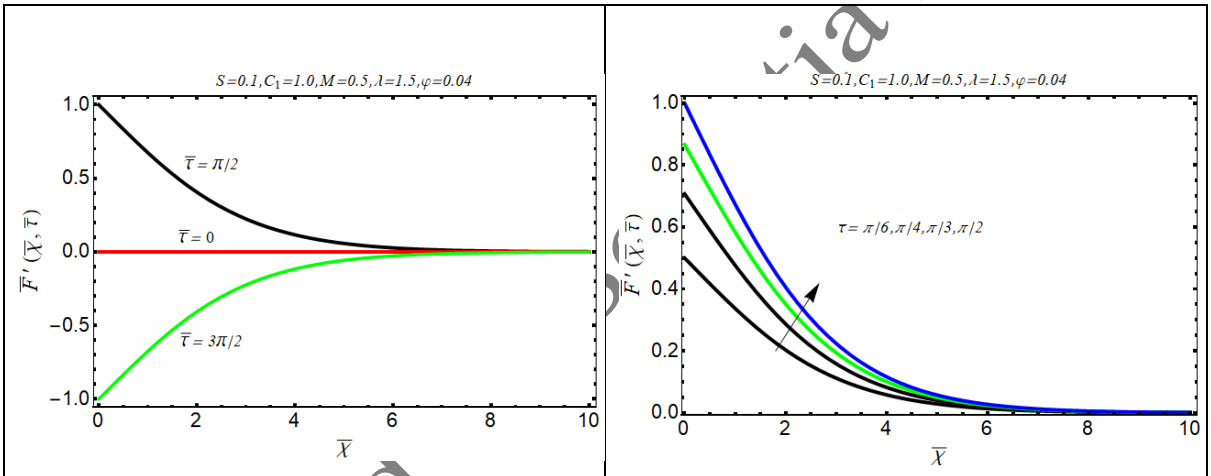

(a) (b)

Figure 8: Effects of $\bar{\tau}$ on $\bar{F}'(\bar{\chi},\bar{\tau})$.

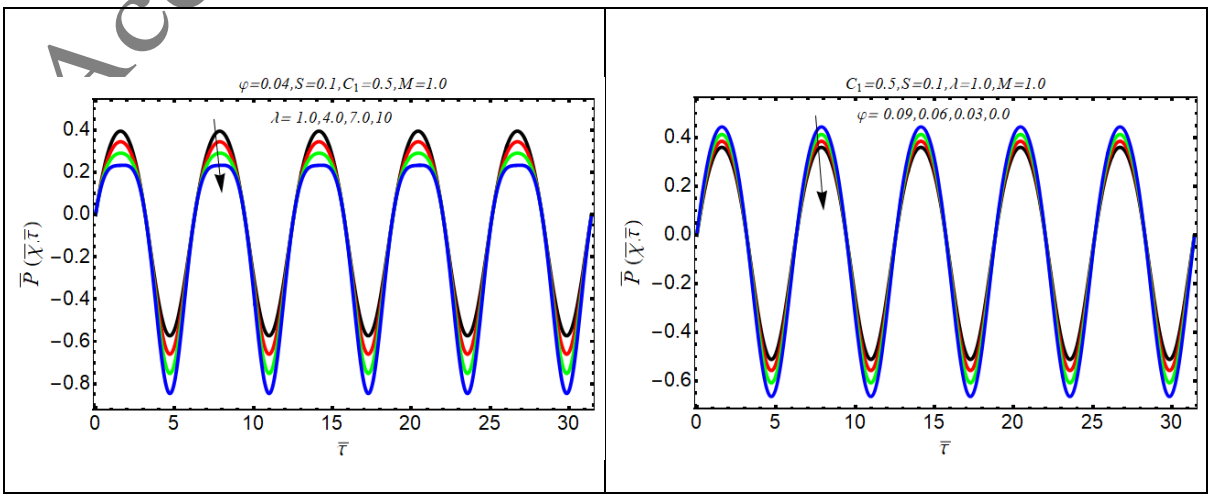

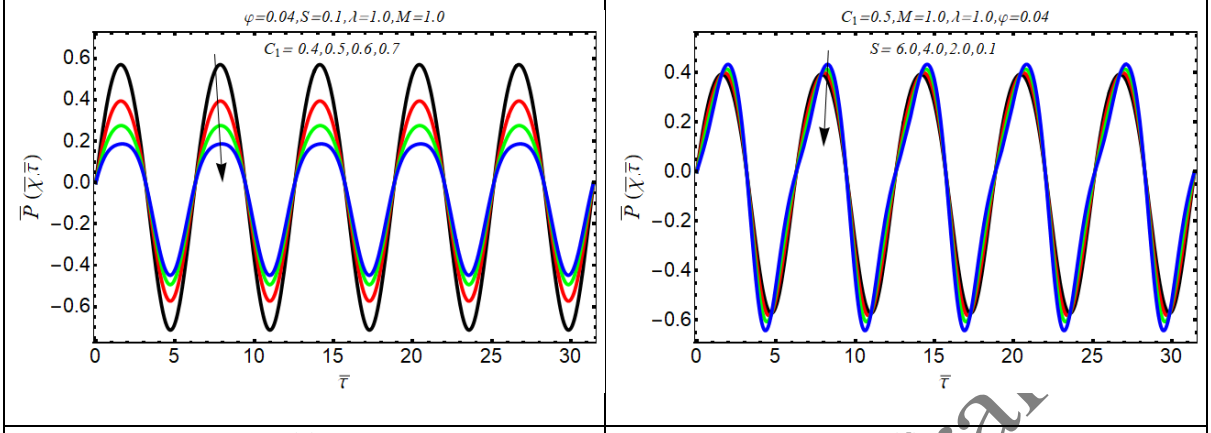

Figure 9: Alteration in pressure profile $\overline{P}(\overline{\chi},\overline{\tau})$.

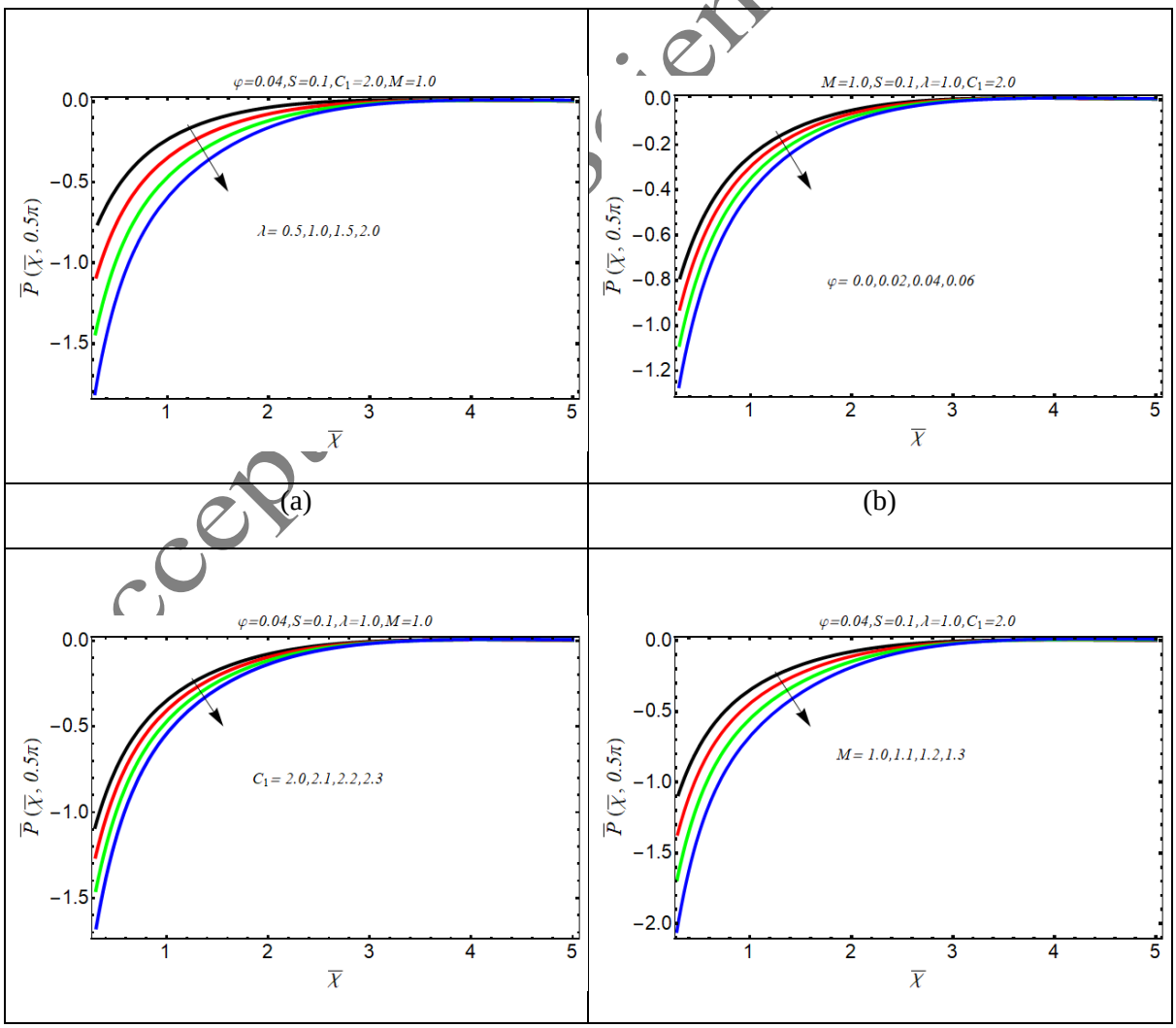

(c)	(d)

Figure 10: Alteration in pressure profile $\bar{P}\left(\bar{\chi},\bar{\tau}\right)$.

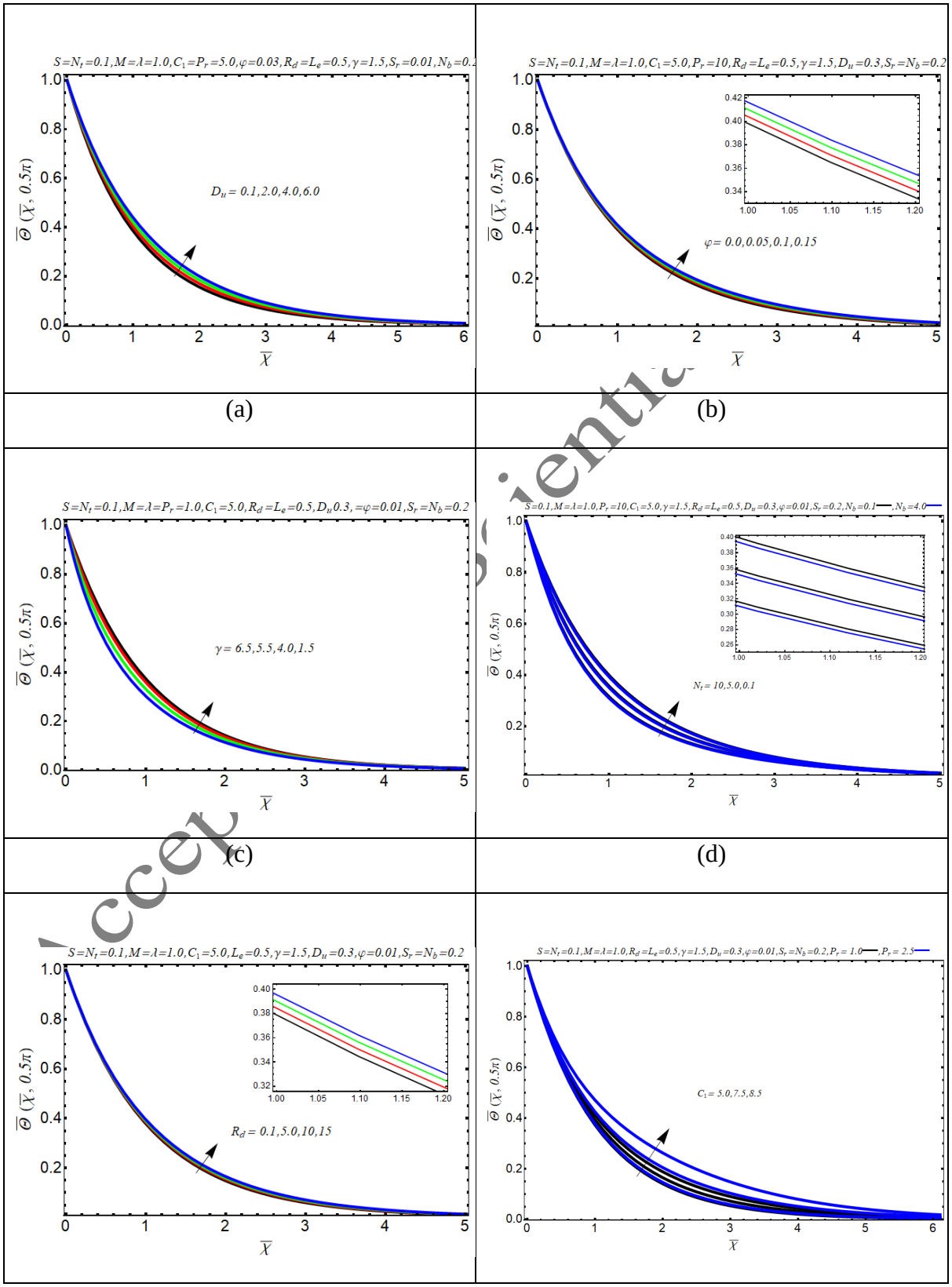

(e)	(f)

Figure 11: Deviation in temperature profile $\bar{\Theta}(\bar{\chi},0.5\pi)$.

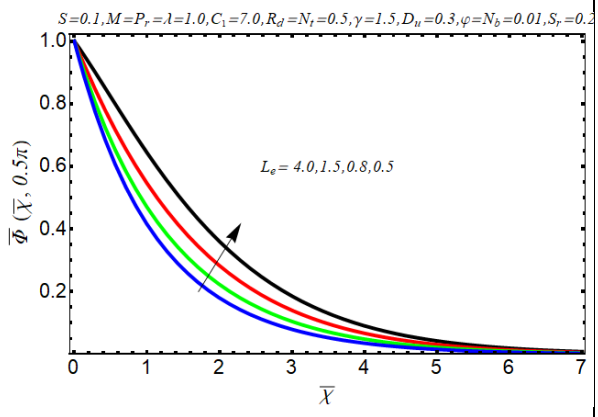

(a)

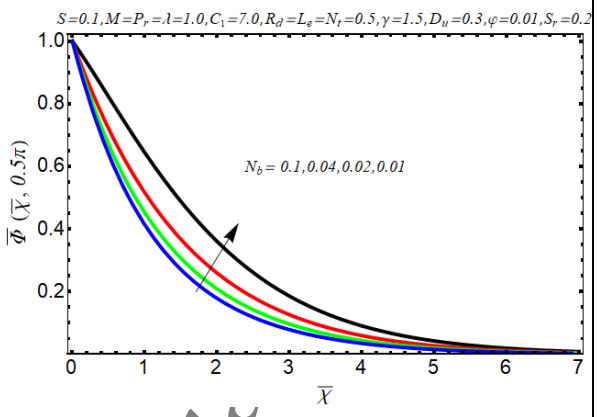

(b)

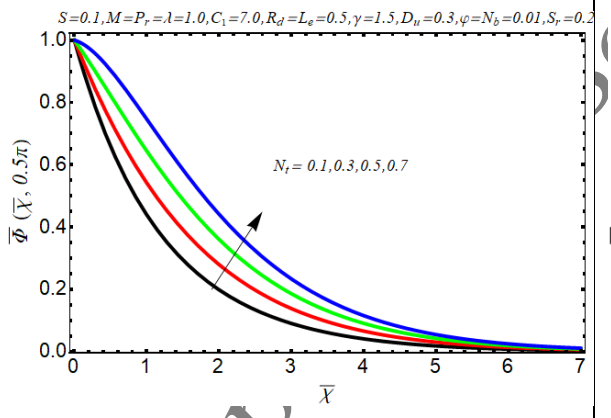

(c)

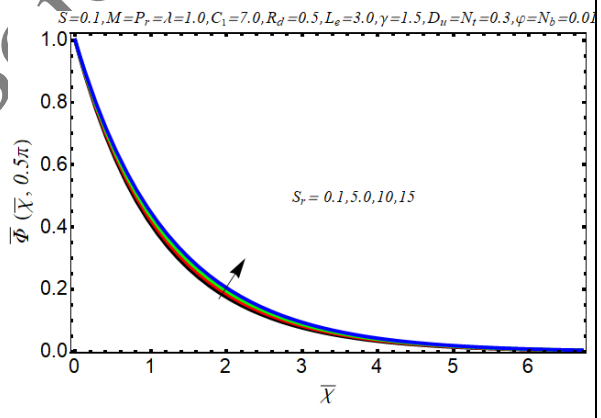

(d)

Figure 12: Deviation in concentration profile $\bar{\Phi}(\bar{\chi},0.5\pi)$

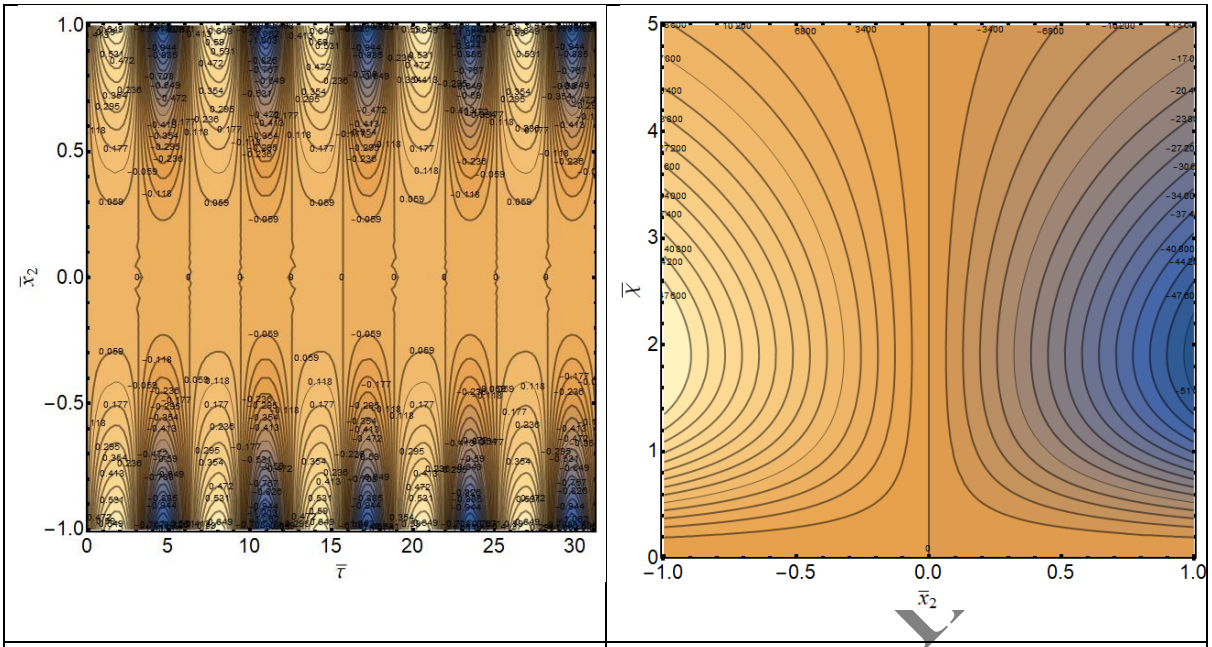

(a) $\bar{\tau} \in (0, 10\pi)$ (b) $\bar{\tau} = 0.5\pi$

Figure 13: Variations in Streamlines of axial velocity component $\bar{w}_1(\bar{x}_1, \bar{t})$.

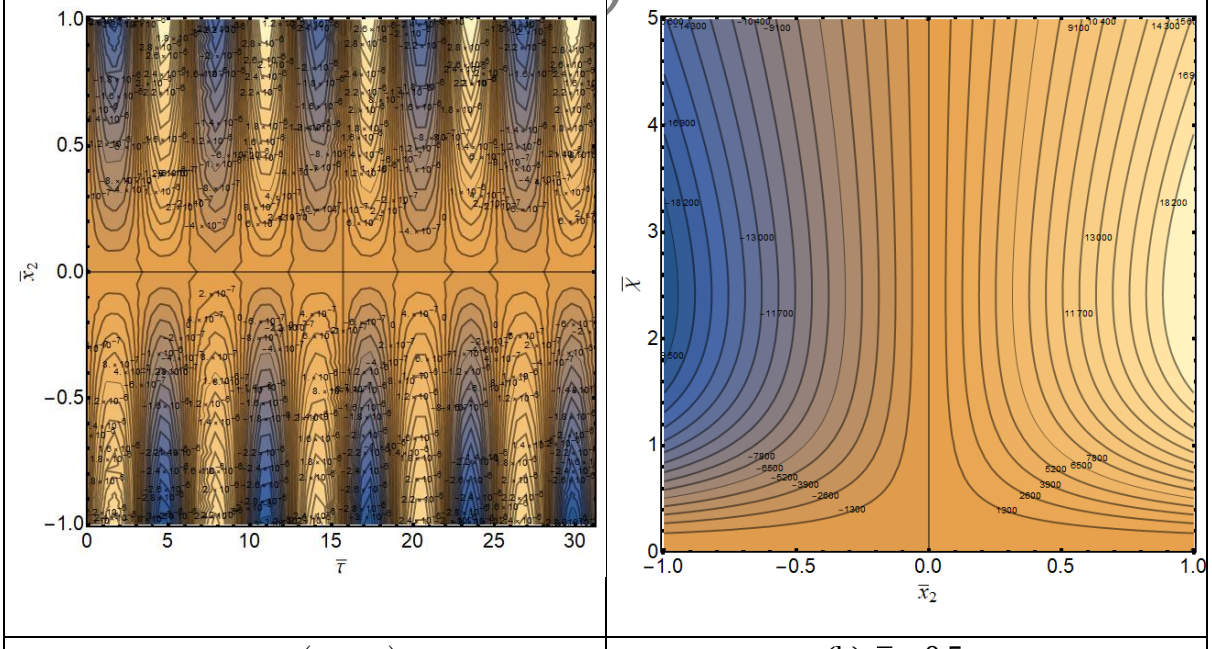

(a) $\bar{\tau} \in (0, 10\pi)$ (b) $\bar{\tau} = 0.5\pi$

Figure 14: Variations in Streamlines of normal velocity component $\bar{w}_2(\bar{x}_2, \bar{t})$.

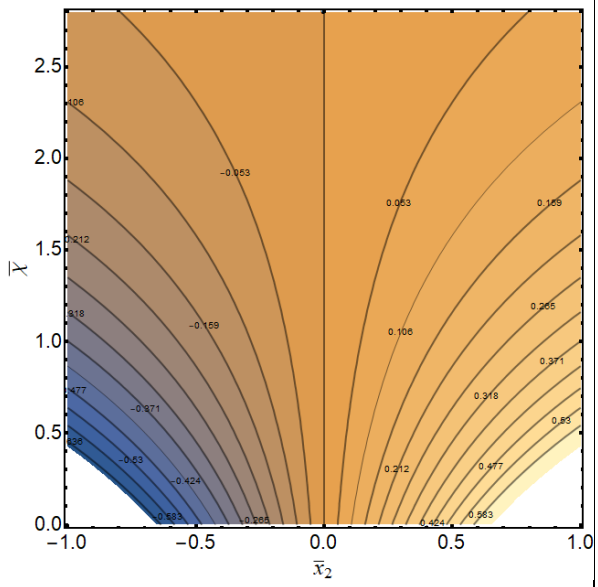

(a) Isotherms

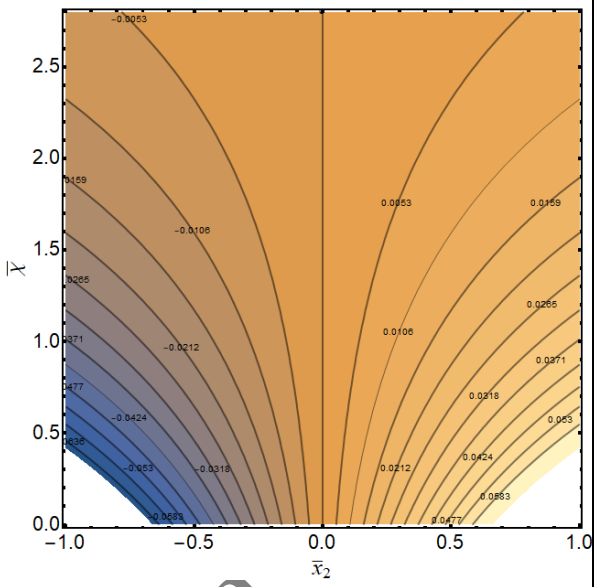

(b) Isoconcentration contours

Figure 15: Variations in Isotherms and Isoconcentration contours when $\bar{\tau} = 0.5\pi$.

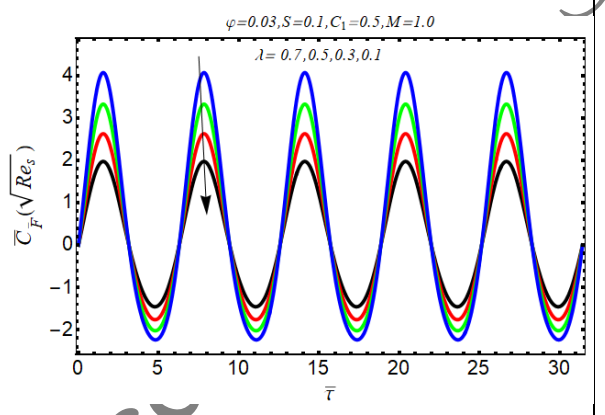

(a)

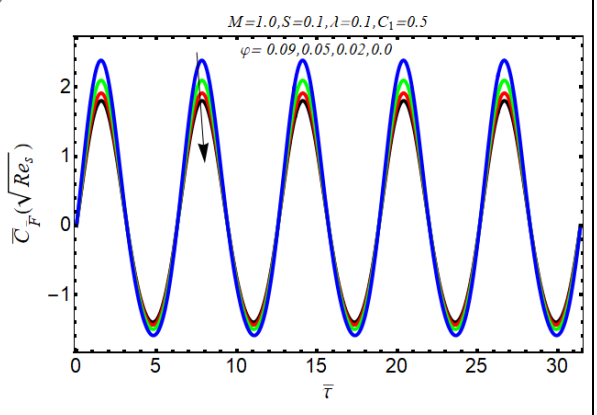

(b)

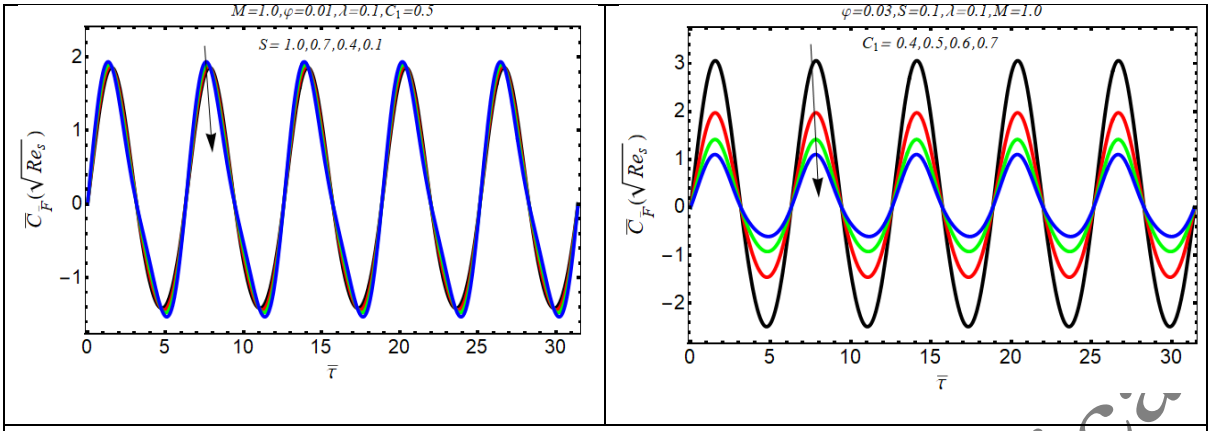

Figure 16: Variation in skin friction coefficient $\left(\bar{C}_{\bar{F}}\left(\sqrt{\mathrm{Re}_s}\right)\right)$.

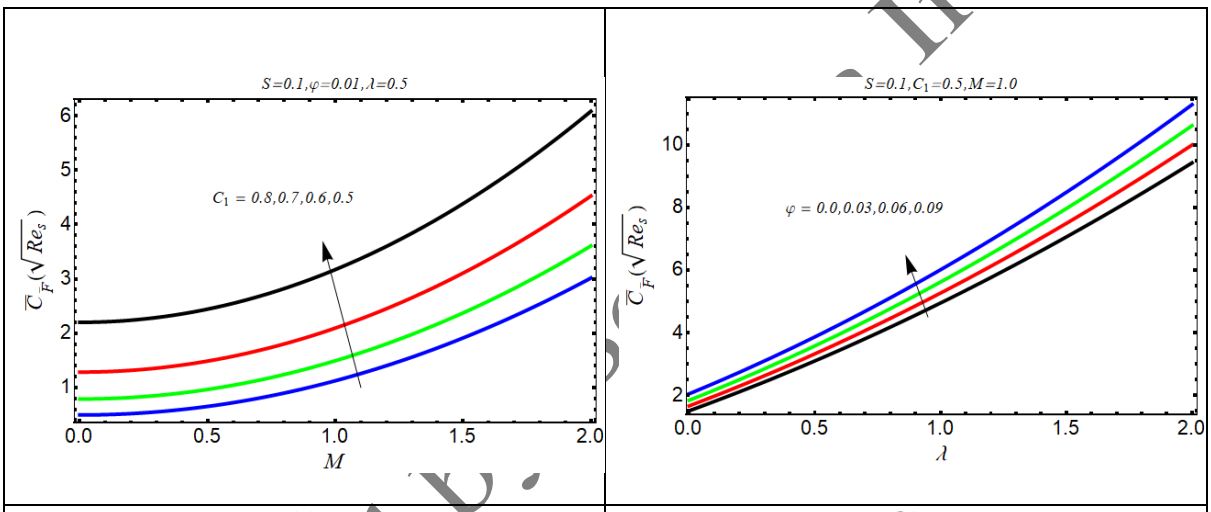

(a) (b)

Figure 17: Alteration in skin friction coefficient $\left(\bar{C}_{\bar{F}}\left(\sqrt{\mathrm{Re}_s}\right)\right)$ when $\bar{\tau}=0.5\pi$.

Table 1: Thermophysical values of the base liquid and nanoparticles [3].

Properties	$\bar{\rho}$	c_p	$\bar{k}$	$\bar{\sigma}$
Base fluid	997.1	4179	0.613	5.5×10^{-6}
Alumina $\left(Al_2O_3\right)$	3970	765	40	3.5×10^{7}

Table 2: Assessment values of $\left(Nu_s / \sqrt{\mathrm{Re}_s}\right)$ for some values of $\left(D_u\right)$, $\left(R_d\right)$, $\left(N_t\right)$, $\left(\gamma\right)$, $\left(C_1\right)$, $\left(N_b\right)$, $\left(\varphi\right)$ and $\left(P_r\right)$ at $\bar{\tau} = 0.5\pi$ when $M = \lambda = 1.0$, $S = 0.1$, $S_r = 0.2$, and $L_e = 1.0$ fixed.

D_u	R_d	N_t	γ	C_1	N_b	φ	P_r	$\left(Nu_s / \sqrt{\mathrm{Re}_s}\right)$
0.1	0.5	0.1	1.5	2.0	0.2	0.02	1.0	2.69057
0.5								2.67418
1.0								2.65369
0.3	0.1							1.35817
	0.4							2.29331
	0.7							3.34839
	0.5	0.2						2.68662
		0.6						2.70361
		1.0						2.72061
		0.1	1.1					1.66492
			1.4					2.36490
			1.7					3.46915
			1.5	1.0				2.75752
				3.0				2.51647
				5.0				1.39332
				2.0	0.1			2.68055
					0.5			2.68784
					0.9			2.69512
					0.2	0.01		2.65631
						0.04		2.73595
						0.07		2.82008
						0.02	0.5	2.69913
							2.0	2.64889
							3.5	2.59871

Table 3: Assessment values of $\left(Sh_s / \sqrt{Re_s}\right)$ for some values of (L_e), (N_b), (C_1), and (N_t) at $\bar{\tau} = 0.5\pi$ when $S = 0.1$, $M = \lambda = P_r = 1.0$, $R_d = 0.5$, $D_u = 0.3$ and $\gamma = 1.5$ fixed.

L_e	N_t	C_1	S_r	N_b	$\left(Sh_s / \sqrt{Re_s}\right)$
0.5	0.2	2.0	0.2	0.1	–0.876851
1.0					–0.936032
1.5					–0.955925
0.1	0.1				–0.620098
	0.3				–0.240064
	0.5				–0.142554
	0.2	0.5			–1.29326
		1.5			–0.701780
		2.5			–0.175271
		2.0	0.1		–0.432298
			0.5		–0.424723
			0.9		–0.417149
			0.2	0.2	–0.619598
				0.5	–0.733106
				0.8	–0.761476

Table 4: Comparison of the numerical results of $\bar{f}''(0,\bar{\tau})$ with existing results for divergent values of $\bar{\tau}$ when $S = 1.0, M = 12, \lambda = \varphi = 0.0$ and $C_1 \to \infty$.

$\bar{\tau}$	Naveed et al. [5]	Imran et al. [23]	Present Results
$\bar{\tau} = 1.5\pi$	11.678656	11.678656	11.678565
$\bar{\tau} = 5.5\pi$	11.678706	11.678706	11.678706

$\bar{\tau} = 9.5\pi$	11.678655	11.678656	11.678655